FACULTY
OF MATHEMATICS
AND PHYSICS
Charles University

BACHELOR THESIS

Orsolya Morvai

Interaction of water vapor with epitaxial layers of cerium dioxide

Department of Surface and Plasma Science, Faculty of Mathematics and Physics, Charles University

Supervisor of the bachelor thesis: RNDr. Břetislav Šmíd, Ph.D.

Study programme: Physics

Specialization: General Physics

2023

I declare that I carried out this bachelor thesis independently, and only with the cited sources, literature and other professional sources.

I understand that my work relates to the rights and obligations under the Act No. 121/2000 Coll., the Copyright Act, as amended, in particular the fact that the Charles University has the right to conclude a license agreement on the use of this work as a school work pursuant to Section 60 paragraph 1 of the Copyright Act.

In Prague, May 9th, 2023 signature

Acknowledgment

I would like to take this opportunity to express my gratitude to my project supervisor Břetislav Šmíd and consultant Xiaohui Ju for their invaluable support and guidance throughout my journey to write this thesis. Furthermore, I would like to thank Peter Matvija for providing the STM images, which enabled a thorough evaluation of the results and the visual representation of the surface arrangement of the prepared samples. Without their help, I would not have successfully been able to complete this task. I am thankful for their patience and support during the measurements and consultations. They were always willing to explain everything several times when I made mistakes, and their commitment to my understanding was evident in every interaction we had. I am also grateful for the great opportunities to work with real, challenging physical problems in the laboratory. These experiences have allowed me to develop my experimental problem-solving skills and gain valuable hands-on experience.

Finally, I would like to thank all those who have contributed to my study in one way or another. I am incredibly grateful to all the professors, colleagues, friends, and family members who have supported me throughout this journey.

Title: Interaction of water vapor with epitaxial layers of cerium dioxide

Author: Orsolya Morvai

Department / Institute: Department of Surface and Plasma Science, Faculty of Mathematics and Physics, Charles University

Supervisor of the bachelor thesis: RNDr. Břetislav Šmíd, Ph.D., ThermoFisher Scientific, Vlastimila Pecha 12, 613 00 Brno, Czech Republic

Abstract:

This thesis investigates the interaction between water and cerium oxide, which, due to its oxygen storage activity, could be widely used in nanomedicine, catalysis, and environmental applications. Despite extensive research, a fundamental understanding of how water interacts with cerium oxide under ambient conditions has been lacking. The study utilizes scanning tunneling microscopy, near-ambient pressure X-ray photoelectron spectroscopy, and the study of water dissociation on stoichiometric CeO_2(111)/Pt(111) thin films with controlled step density. The results demonstrate the identification of three adsorption species and reveal that the dissociation kinetics depend on step density. These findings provide new insights into the role of water in cerium oxide interactions under operando conditions.

Keywords:

NAP-XPS, cerium oxide, water vapor, controlled step density, operando studies

Contents

1. Introduction

In recent years, the development of new materials with improved properties has been a topic of great interest in the field of material science. A promising approach to improve the properties of materials is to modify their surface characteristics. To gain a better understanding of the chemical and physical properties of surfaces, various analytical techniques have been used, including X-ray photoelectron spectroscopy (XPS).

However, XPS is generally limited to study materials under ultra-high vacuum (UHV) conditions – typically in the range of 10^{-8}-10^{-10} mbar [1], which can be significantly different from the environment in which the studied material is used or processed in real life at ambient pressure. Also, some sample properties can be changed when exposed to UHV conditions so the measurements performed with XPS may not accurately reflect the surface properties of the materials. Therefore, Near ambient pressure X-ray photoelectron spectroscopy (NAP-XPS) has emerged as a powerful tool to study the surface chemistry of materials under near-realistic conditions. It operates typically in the range from 10^{-6} to a few tens of mbar [2]. NAP-XPS made it possible to study materials in gas or liquid environment in the form of vapor, including the quasi-dynamic changes in surface chemistry during chemical reactions with the environment under partial pressure conditions.

This thesis will focus on the use of NAP-XPS to study the surface properties of cerium dioxide (CeO_2) – further in the text is simply referred to as cerium oxide or ceria – during water vapor exposure. Cerium oxide (CeO_2) is a material that has been widely investigated due to its unique physical and chemical properties and its application possibilities such as electrochemistry, catalysis [3], and green energy [4]. Lately, the application interests have been extended to the nanomedical field [5] [6] because of its similarity to natural enzymes [7] [8] [9] in catalyzing redox reactions. In particular, CeO_2 has been found to exhibit certain interactions with water molecules. This interaction can significantly affect the CeO_2 behavior in various applications since water vapor is one of the most abundant molecules in ambient conditions [10][11]. The above-mentioned possible applications are based on the unique physical/chemical

properties of cerium oxide, such as the high oxygen storage capacity (OSC) [12], good thermal stability, and excellent redox properties. It remains unclear how the surface of CeO_2 interacts with water molecules under ambient conditions, thus the effect of the water on these chemical properties can raise important questions in mediating their potential applications. The electronic structure of CeO_2 can be modified by the adsorption of water molecules on its surface. The presence of water molecules on the surface of CeO_2 can lead to the formation of different surface states, which can affect its electronic conductivity, its ability to exchange electrons with other materials, and its oxygen storage capacity, as the hydroxyl groups formed on the surface of CeO_2 can affect the redox properties of the material. The presence of water vapor can significantly affect the catalytic activity of CeO_2, as it can lead to the formation of new active sites on the surface of the material. The thin layer of water on oxide surfaces can be formed by adsorption, dissociation, or even possible reductive reactions. The water layer thickness created on the surface of cerium oxide depends on the strength of the chemical bonds between CeO_2 and water molecules and on the hydrogen bond between adsorbed water layer and gas phase water. The strength of the chemical bonds depends on the ceria surface topology in which the step-edge formations on the surface play a major role.

Since the oxygen storage capacity arises from reversible conversion between the two different oxidation states (Ce^{3+} and Ce^{4+}), and the Ce^{3+} state is the one with the less probability, it is important to influence the balance between them to affect the electronic structure and reactivity of the material. When Ce^{4+} ions are transformed into larger Ce^{3+} ions the resulting geometric distortions in the ceria lattice are more effectively accommodated at step edges than on the flat, ideal surface [11]. A step edge is a line defect on the surface of a material that separates two terraces with different heights. and Step edges may play a significant role in the surface properties of materials such as their reactivity, adsorption, and diffusion behavior. Since the oxygen storage capacity arises from reversible conversion between the two different oxidation states (Ce^{3+} and Ce^{4+}), and the Ce^{3+} state is the state with the less probability, it is important to influence the balance between them to affect the electronic structure and reactivity of the material.

As for the water-ceria interaction, it is important to include the temperature and the pressure among the variables. In the past, the interaction between CeO_2 and water has been extensively studied by XPS under UHV conditions. Because of the pressure gap between the UHV conditions and the ambient conditions, a solid state of water (ice) [13] [14] was usually formed during the UHV experiments. As ice may form different hydrogen bonding networks during adsorption, differences in the interaction between cerium oxide surfaces and water under different pressure conditions (e.g., ice with an ordered hydrogen bond network or water vapor with random weak hydrogen bonds) are suspected to exist. Also, keeping the observed sample at different temperatures can make a difference in the water chemistry of cerium oxide, not to mention the morphological differences of the sample surface, including terraces and step edges.

In this thesis, we will try to consider most of the changing variables to make complete predictions about the water interaction with the epitaxial cerium oxide (111) thin film surface, including CeO_2(111) step density, reaction water vapor pressure, and reaction temperature. During the experiments, we will try to figure out whether the water vapor is molecularly adsorbed or dissociated as the first monolayer on fully oxidized cerium oxide, and we will also further study the amount of hydration/hydroxylation of CeO_2 under near ambient conditions. We will also study different layer structures using stoichiometric surfaces with controlled step edges and compare their reactivity with water vapor molecules by experimental technique NAP-XPS.

In summary, CeO_2 is a promising material with exceptional physical and chemical properties that make it attractive for various applications in material science. Considering the changing variables such as pressure, temperature, and step edges, we will gain a complete picture of CeO_2 and water interaction and investigate the water adsorption/dissociation processes on the surface under ambient pressure conditions. We conclude that the hydration/hydroxylation process of CeO_2 under ambient pressure can significantly affect its physical and chemical properties, including its catalytic activity, oxygen storage capacity, and electronic conductivity. The insights gained from this thesis will have significant implications for the development of materials with improved properties for a wide range of applications.

2. Experimental methods

2.1 X-ray photoelectron spectroscopy

The most important method used in this thesis was a surface-sensitive analytical technique called X-ray photoelectron spectroscopy (XPS). It was developed by a research group led by Professor Kai M. Siegbahn at the University of Uppsala in 1954 Professor Siegbahn was awarded the Nobel Prize in 1981 for his contribution to the development of XPS. The first commercial XPS setup was developed at Hewlett Packard in 1969 [15].

XPS is based on the photoelectric effect explained by Albert Einstein in 1905. In general, the theory states that if a surface is irradiated by light particles with a sufficiently high frequency, electron emission can be observed. In the case of XPS analysis, X-ray radiation obtained from an aluminum anode is used as the light source. After the surface atoms adsorb the energy carried by the X-rays, photoelectrons near the surface of the sample escape into the vacuum. The kinetic energy of the photoelectrons depends on the energy of the incident radiation and the binding energies of the electrons, which are specific to the analyzed material and the level of the atom from which the electron came. Figure 2.1 represents the different photon/electron emissions.

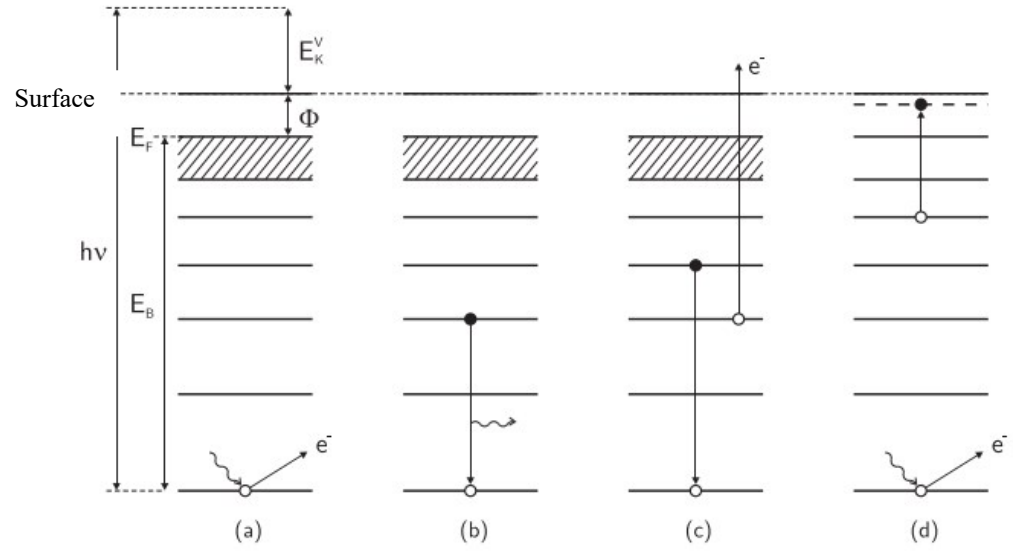

Figure 2.1: Schematic representation of (a) photoemission from the solid-state atom's inner shell and of deexcitation processes: (b) photon emission (fluorescence), (c) Auger process, (d) shake-up transition [16].

The kinetic energy of the emitted electron can be denoted as E_k^v and $h\nu$ is the X-ray radiation energy used. The relation between the two quantities is as follows:

$$h\nu = E_k^v + E_B + \phi, \tag{2.1}$$

where E_B denotes the electron's binding energy. The quantity ϕ is a work function-like term that is significant in the case of a material with a specific surface, and a small correction because of the instrument's contact potential needs to be considered. Overall, ϕ is a constant that sometimes appears in practice [17]. From equation (2.1) the binding energy can be expressed as:

$$E_B = h\nu - E_k^v - \phi \tag{2.2}$$

After the first electron emission, the atom enters an unstable and ionized state. The remaining electrons are influenced by the change in the field, so the binding energy is further modified by a factor called the relaxation energy E_{relax}.

$$E_B = h\nu - E_k^v - \phi - E_{relax} \tag{2.3}$$

The instability leads to deexcitation, which can occur in two different ways. First, another electron from a higher energy shell can replace the emitted electron in a radiation process called fluorescence. Alternatively, the surplus energy can be transferred to another electron, which is called an Auger electron.
Another process is called the shake-up process, which occurs when electrons from the valence band (whose energy levels are expected to be discrete) are excited by the resulting potential, causing higher energy states to appear in the spectrum.

In the following part, the operating process of X-ray photoelectron spectroscopy will be described. The standard setup for XPS method is depicted in Figure 2.2.

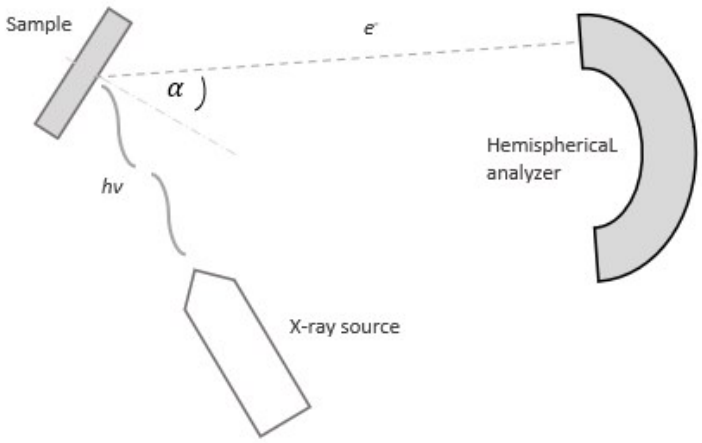

Figure 2.2: A simplified scheme representing the mechanism of XPS – The X-ray radiation interacts with the sample, causing electrons to be emitted from the surface (due to the photoelectric effect). These emitted electrons are subsequently detected by a hemispherical analyzer.

Firstly, X-ray radiation is obtained from $Mg\ K_\alpha$ or $Al\ K_\alpha$ anodes in an X-ray source. The generated light then hit the sample and interacts with the surface. Some of the photoelectrons from the surface reach the spectrometer, which has mostly a hemispherical shape. In the hemispherical spectrometer, electrons move between two spherical electrodes in a radial electromagnetic field. Referring to the Lorentz force, its effect is described with the following equation:

$$\vec{F} = q(\vec{E} + \vec{v} \times \vec{B}) \qquad (2.4)$$

It is known that the electrons are going to move on a circular path. The radius of their circular paths is velocity dependent, so the hemispherical capacitor separates the electrons by their speed. At the end of the route, the electrons reach the multi-channel detector. The detector detects the place of their impact thereby obtaining information about speed.

As described previously, the velocity of the electrons is a function of the binding energy, so as the output, an energy spectrum can be obtained. The binding energy is

directly related to the chemical properties of the atoms and molecules, including their proton number and chemical oxidation states. Therefore, by analyzing the obtained spectra, information about the chemical environment of the surface can be obtained.

An important point is the “analyzed thickness” of the surface, or the information depth, representing which the information is gained from. Although X-ray radiation has a penetration depth on the order of micrometers, the escape depth of electrons in a solid sample is limited to only a few nanometers. This is due to the fact that electrons are heavier than light particles and are more likely to be absorbed by other atoms, resulting in a shorter escape depth.

When the sample surface is not perpendicular to the optics of the hemispherical analyzer, the information depth is smaller than the escape depth. The magnitude of the information depth is inversely proportional to the angle between axis of the optics of the analyzer and the normal vector of the surface, denoted as α. The relationship between the escape depth and information depth is depicted in Figure 2.3.

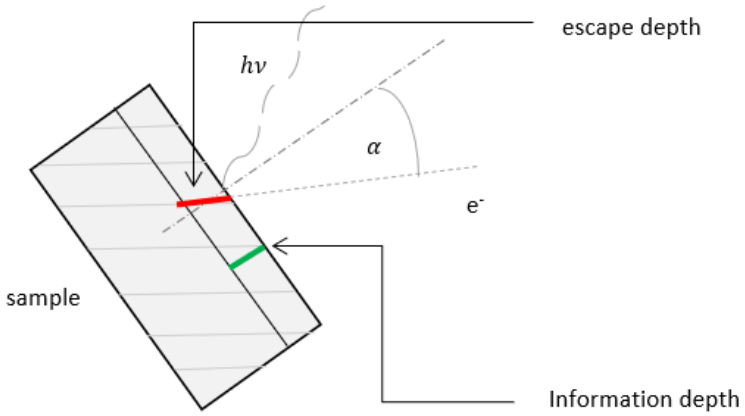

Figure 2.3: Illustrative representation of escape depth and information depth

As analyzing the obtained spectrum from the measurement, a function of electron intensity with respect to the binding energy is generated. This spectrum depicts the occurrence of electron intensity peaks, which indicate the number of escaped electrons

from different atomic levels. The processes occurring include fluorescence radiation, Auger transitions, shake-up processes, and energy loss peaks. Each atom has a unique spectrum, which enables the estimation of the chemical composition and chemical state of the measured surface. The intensity of these peaks is dependent on the effective cross-section for photoionization, inelastic mean free path, sample material, and the transmission of the spectrometer at a specific kinetic energy [16].

2.2 Near ambient pressure X-ray photoelectron spectroscopy

Conventional XPS measurements are carried out in the UHV conditions as mentioned previously. This sometimes results in analyzing samples that are significantly different from their natural environment under ambient pressure conditions, leading to inaccuracies in the analysis. To address this limitation, an advanced instrument based on the XPS principle was developed that can operate under higher pressure conditions. This has allowed the analysis of samples under conditions closer to the ambient pressure as well as studying material interactions with gas molecules under operando conditions.

Although Kai Siegbahn was experimenting with XPS under higher pressures and in the presence of liquid vapors already in the 1970s, NAP-XPS was introduced in 2001 by H.-J. Freund and his colleagues at the Fritz Haber Institute in Berlin, Germany. NAP-XPS is built upon the basic concept of XPS whose operation has been described previously in this chapter, with the main difference of being able to work under higher pressures, approaching ambient levels.

Since electrons are likely to interact with other particles, the standard XPS method usually operates under UHV conditions to avoid the loss of photoelectrons. In the case of high-pressure measurements, a specific cell (near ambient pressure cell, or NAP cell) with sufficient pressure isolation is required. This cell keeps most of the high pressure inside its compartment while allowing the electrons to evacuate through a small aperture to the pumping stages and further reach the analysis chamber. The hemispherical spectrometer can only operate under UHV conditions. Since there is a

residual pressure leak in the analysis chamber, contrary to a conventional XPS setup, a triple-stage pumping system is needed before the photoelectrons enter the analyzer. Due to the nature of the methodological setup, the spectrum intensity is much lower, and the noise-to-signal ratio is higher. This is due to the small aperture and the gas atoms with which the photoelectrons interact until they leave the NAP cell. Nevertheless, with the right alignment, informative spectra can be obtained to effectively examine the material interaction with a high-pressure gas medium.

2.3 Low energy electron diffraction

Another important surface science analysis technique is called low energy electron diffraction (LEED) [18]. This method is mainly used for the structure analysis of a crystal's surface by diffraction. According to the particle-wave duality mechanism, diffraction spots are generated due to the interaction between electrons and the crystal surface. These diffraction spots correspond to the inverse space of the crystal structure and are the results of the wave-like nature of the electrons as particles. The surface structure can be qualitatively determined by observing the symmetry and rotation of the diffracted beam pattern or quantitatively by the intensities that appeared on the screen. The electrons used in the LEED experiment are typically in the energy range of 20-200 eV [18].

In crystals, the atoms are periodically arranged, except for some crystal defects. It was known for a long time that after sending light on a diffraction grating, the light diffracts, due to the wave properties of light. In 1924 it was discovered that not only light has wave properties, but mass particles like electrons and protons as well [19]. In the 1960s LEED became a popular method and it has been used for studying the structure of crystal surfaces. By this method, two basic spaces can be distinguished, first is the crystal space, and secondly the reciprocal (diffraction) space. The relations between these two spaces are given by the Laue diffraction conditions:

$$\vec{a}_1 \cdot \vec{q} = 2\pi h \qquad (2.5)$$

$$\vec{a}_2 \cdot \vec{q} = 2\pi k \qquad (2.6)$$

$$\vec{a}_3 \cdot \vec{q} = 2\pi l \qquad (2.7)$$

Where $\vec{q}$ is the difference between the wave vector of the diffracted wave $\vec{k_f}$ and the wave vector of the incident wave $\vec{k_i}$, respectively:

$$\vec{q} = \vec{k_f} - \vec{k_i} \qquad (2.8)$$

The simplified LEED experiment setup is represented in Figure 2.4:

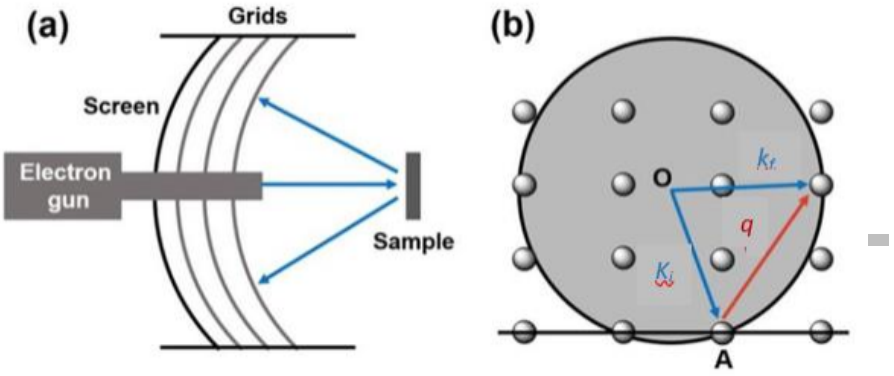

Figure 2.4: (a) LEED setup. (b) Ewald sphere construction [20].

The Ewald sphere plays a crucial role in the efficiency of the mentioned principle because diffraction occurs only on the lattice points that lie on the Ewald sphere surface. The radius of the Ewald sphere depends on the inverse of the wavelength of the incident radiation. The low electron particles, thanks to their short wavelengths, exhibit an Ewald sphere with a greater radius than X-ray waves in X-ray diffraction. Due to this side effect, there is a higher chance that the sphere will intersect the grid points of the reciprocal space.

2.4 Quadrupole mass spectrometry

As a control of gas distribution/quantification in the NAP cell during XPS measurements, an instrument called quadrupole mass spectrometry (QMS) was further

integrated into the NAP-XPS station. It has been used mainly to observe the partial pressure changes of different gases in the cell. Thanks to this method, one can estimate the background gas composition during the NAP-XPS measurement, and a complete evolution of the pressure changes can be monitored for all the gases in the cell.

The first quadrupole mass spectrometer was developed by W. Paul (shared Nobel Prize in Physics, 1989) in the early 50s and it is based on a design applying alternating quadrupolar electric fields to solve the deficiencies of a spectrometer using a magnetic field. [21] It consists of an ionizer, an ion accelerator, and a mass filter, which consists of four metal rods. The rods have an applied periodical potential $\pm(U + V\cos\omega t)$, where U is the direct current, and V is the alternating current. Two diagonal rods have the same voltage, while the other two have the same magnitude but with opposite signs. The voltage of the rods is varied, and due to this variation, only ions of a certain mass-to-charge ratio can pass through the quadrupole filter [22].
The scheme of a quadrupole mass analyzer is represented in Figure 2.5.

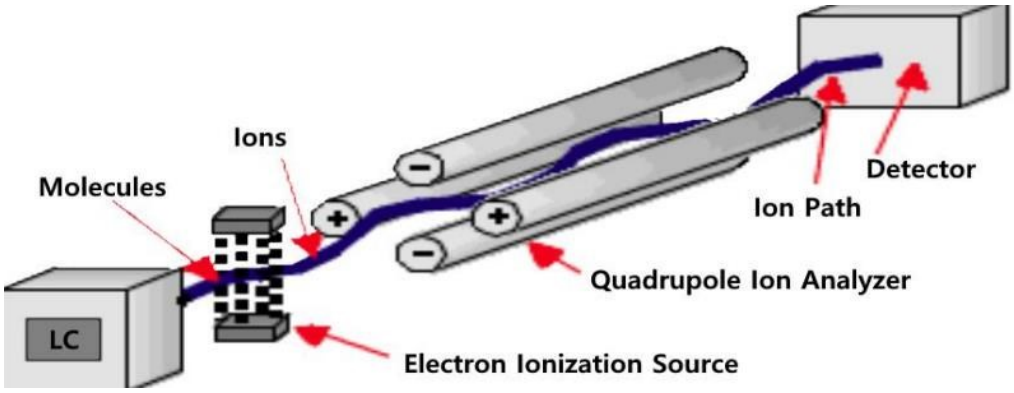

Figure 2.5: Schematic representation of QMS [22].

2.5 Scanning tunneling microscopy

Thus far, the techniques described have enabled the observation of the chemical composition (through XPS) and crystal structure (by LEED) of the surface as well as analyzing the gas composition after interacting with the surface (with QMS). However, for a more comprehensive understanding, it is essential to determine the surface

morphology of the sample, as well as the number of step edges presented on the surface. Hence, a technique known as scanning tunneling microscopy (STM) will be used in this thesis.

The principle of STM is based on the quantum physical phenomenon called quantum tunneling. This phenomenon is explained by the Heisenberg uncertainty principle and the wave-particle duality. It occurs at the quantum scale, where particles are described by spatial wave functions, and they have a small probability of occurring beyond a higher potential energy barrier than their energy [23]. The above-described phenomenon is illustrated in Figure 2.6.

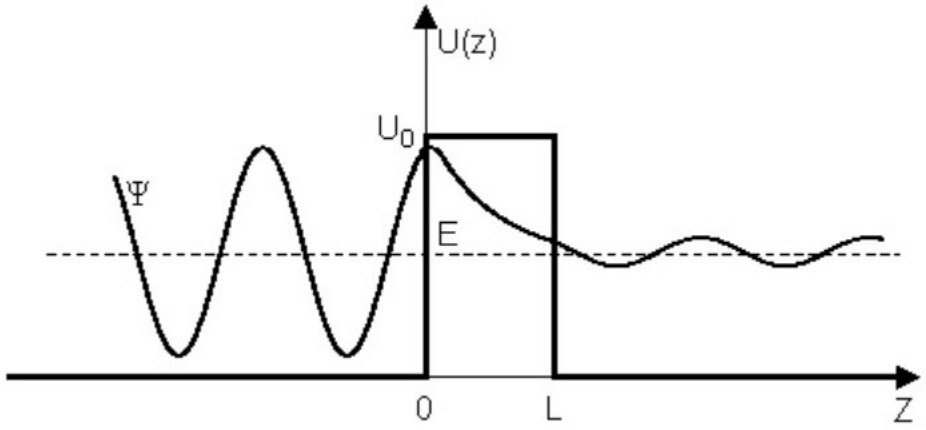

Figure 2.6: Schematic representation of the tunneling phenomenon [23] - the potential energy barrier is denoted by U_0. Given the wave-particle duality, there is a probability that the mass particle appears on the other side of the barrier, despite having lower energy than U_0.

The experimental scheme of the measurement method is represented in Figure 2.7. The main component of the equipment is a sharp, thin tip, which is typically made of a metal wire, such as tungsten or platinum-iridium alloy. The tip is typically coated with a thin layer of conductive material, such as gold or silver, to improve its electrical properties. The distance between the sample and the tip is on the order of atomic size, which is approximately 10^{-10} m. After creating a voltage between the sample and the tip, a small current is produced due to the quantum tunneling phenomenon. The size of this current is strongly correlated with the surface topography. STM maps the surface of a sample by maintaining a constant distance between the sharp tip and the

sample. The differences in tunneling current, which are sensitive to the distance between the tip and the sample, are measured to create a detailed map of the surface topography at the atomic scale. Alternatively, the tip-sample distance can be adjusted while maintaining a constant current to directly measure the surface topography. The STM enables visualization and manipulation of the atomic structure of a material with remarkable precision [18].

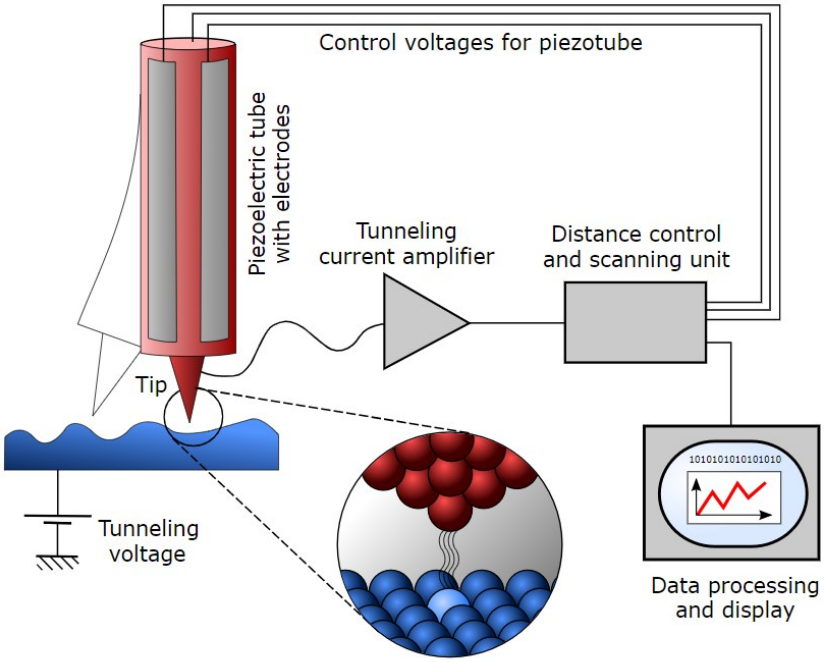

Figure 2.7: Schematic representation of the STM method [24].

By reconstructing a two-dimensional image from the measured data, obtained from the mapped surface area using STM, a colormap-like figure can be generated. This figure is indicative of the surface morphology and topography and atom arrangement presented on the surface.

2.6 Step edge density calculation

F. Dvořák's method [16] was utilized to calculate the density of step edges on the surface of $CeO_2(111)$ using obtained STM images. In this method, the density of steps is determined by counting the number of Ce atoms present at the step edges of cerium oxide islands. Briefly, the step edges were marked with a one-pixel-wide line, and a

mask image was generated. Equation (2.9) was used to determine the length of step edges in nanometers (nm), with the total number of pixels (N) being used for this calculation.

$$L = k \times N \times (\frac{W_{nm}}{W_{px}}) \quad (2.9)$$

The width of the analyzed image was considered while calculating the length of step edges. Specifically, the width of the image was measured in both pixels (W_{px}) and nanometers (W_{nm}). An analytic coefficient (k = 1.134) was incorporated to account for the correction required due to the various directions of surface steps with respect to the pixel orientation on the screen. The number of atoms presented at step edges (N) was determined using the equation (2.10):

$$N = L/a \quad (2.10)$$

where a = 0.382 nm is the lateral interatomic distance in CeO_2(111) plane.

The density of steps on the CeO_2 surface (d_{CeO2}) was obtained using the following relation:

$$d_{CeO2} = N/(S_{nm} \times n) \quad (2.11)$$

where S_{nm} is the area of analyzed image and n = 7.91 atom/nm^2 is the number of cerium atoms in the CeO_2(111) plane.

As an example, one concrete calculation with the masked image will be shown in the layer preparation and characterization chapter (4. Chapter, 4.1 Section).

3. Experimental setup

In the following section, the equipment setup and experimental conditions will be described.

The NAP-XPS setup was provided by SPECS (SPECS Surface Nano Analysis, GmbH). The equipment consists of several parts, incorporating other measurement systems to provide a thorough surface analysis of the sample of interest. The schematic pictures of the equipment are represented in Figures 3.1-3.3. In these figures, the main parts of the setup are highlighted in red circles. As shown in the following illustrational figures, the experimental setup is also equipped with complementary analyzing systems such as LEED and QMS.

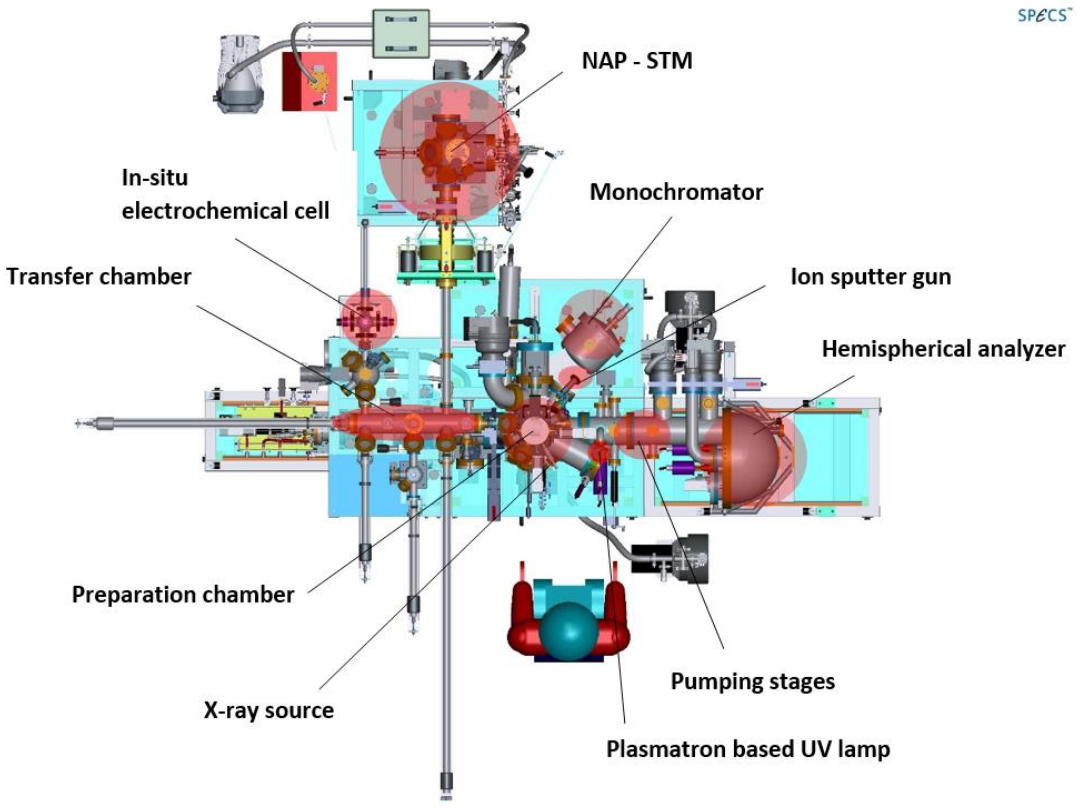

Figure 3.1: Schematic illustration of the experimental setup from the top view (Credit: SPECS, GmbH).

The equipment has two levels, so the parts below the transfer and preparation chamber level are not visible in Figure 3.1. However, in Figure 3.2, a different point of view of the same equipment is shown, which displays the parts located on the lower level.

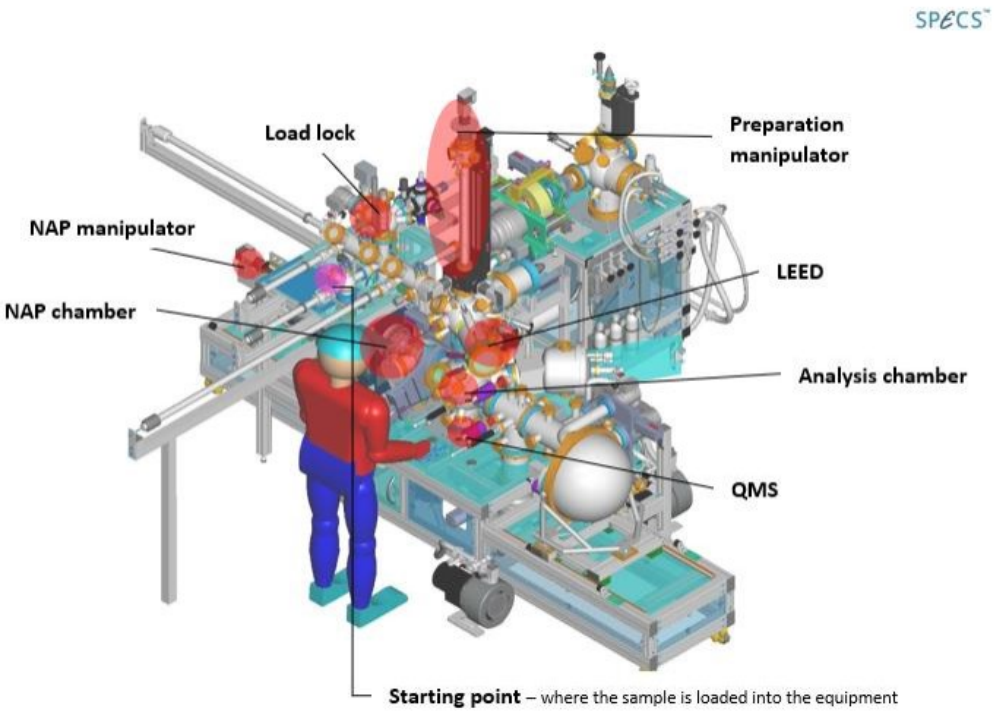

Figure 3.2: Schematic illustration of the experimental setup viewed from the side. (Credit: SPECS, GmbH).

Figure 3.3 shows a schematic illustration of the NAP cell, which is connected to the analyzer (hemispherical capacitor) through the differential pumping system. The figure also highlights the assigned pressures for each stage. During a near-ambient pressure measurement, the NAP cell is moved into the analyzer chamber by the NAP manipulator. The sample is relocated to a holder inside the NAP cell. The sample temperature during the measurements can be adjusted between 280 K and 670 - 923 K (depending on the used gas and pressure) through incorporated heating elements.

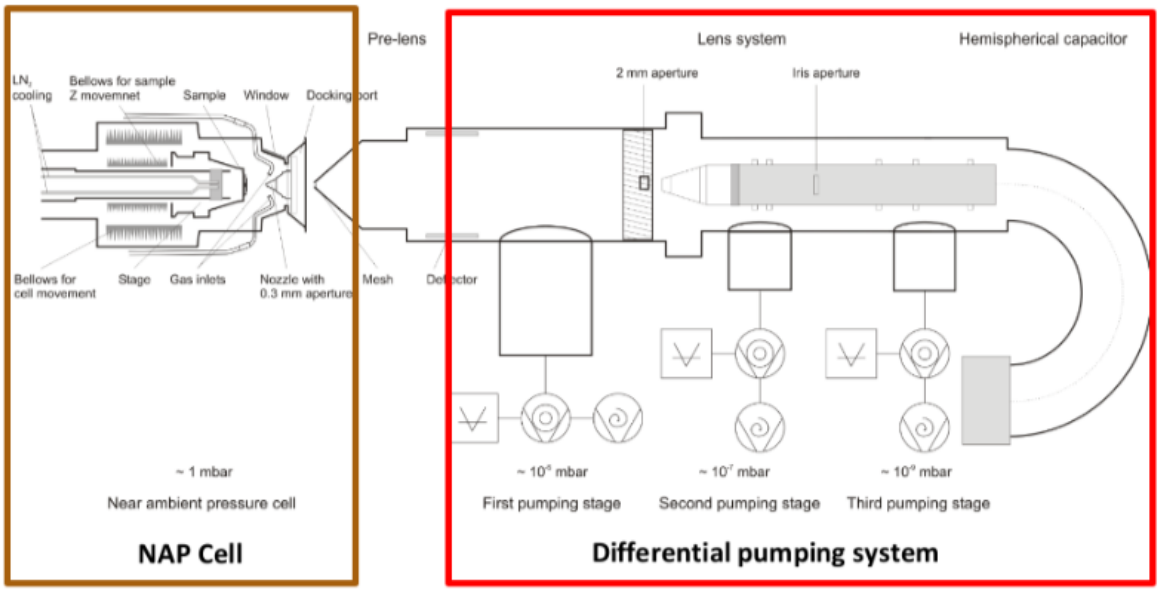

Figure 3.3: Schematic representation of the NAP cell and the differential pumping system with the hemispherical analyzer.

Prior to the measurement, the sample needs to be loaded into the equipment. The location where it can be loaded is highlighted in Figure 3.2, denoted as the starting point. When conducting XPS measurements, the sample on a sample holder is transferred from the starting point to the preparation chamber through the transfer chamber, where it can be placed on the preparation manipulator. All the manipulators are operated by a computer program from SPECS (SpecsLab Prodigy). The different chambers are separated by gate valves, allowing for independent pressure observation and regulation. The preparation chamber is used for layer growth and cleaning processes, and also the LEED equipment is installed on this chamber. It is possible to control the sample temperature within a range of 260 K to 1100 K (1300 K with a specific holder) via the thermocouple on the preparation manipulator. During the measurement, the sample is located in the analysis chamber where the X-ray source is also integrated. For the measurements, $Al\ K_\alpha$ radiation is utilized, which has an energy of 1486 keV. The exact position of the sample is adjusted by the computer program, and it remains on the preparation manipulator throughout the measurement process. The surface area exposed to the X-ray photons can be adjusted, along with the spot size of the X-ray beam. After the photoelectrons leave the surface with a certain

velocity, they reach the analyzer where their energies are measured. The resulting spectrum shows the electron intensity as a function of binding energy (as described in the theoretical part of the thesis). From the preparation chamber, the sample can be manually relocated to the load-lock chamber or the STM chamber via manual transfers.

The data fitting was performed using a program KolXPD (J. Libra, KolXPD: Software for spectroscopy data measurement and processing [25]). As a first step, it is important to select a proper background. There are three types of measurement backgrounds typically used in XPS method: Linear, Shirley, and Tougaard. To remove a linear background, a given value is subtracted from the electron intensity at each binding-energy point. The subtracted value is derived from a linearly decreasing function that corresponds to the minimum intensity points of the spectrum. The Tougaard background is based on a physical model that describes the inelastic scattering properties of the material [26]. The background used in this study was the Shirley background, which assumes that the background intensity at a given energy is proportional to the total intensity at higher energies [26]. The subtraction process is iterative and is governed by the following equation:

$$F^n(E) = J(E) - k_n \int_E^{E_{max}} F^{n-1}(E')dE' \qquad (3.1)$$

Where n stands for the iteration order, E is the binding energy and the k_n is the parameter for optimization. The nth order F function represents the spectrum obtained after n steps. Therefore, the measured spectrum is equivalent to the zeroth order F function $J(E) = F^0(E)$. The algorithm stops immediately, when $F^n(E_{min}) = 0$. The convergence is reached rapidly, usually three or four-iteration order is needed. E_{min} and E_{max} are the low energy boundary of the peak and the high energy boundary of the peak, and they are chosen by the user before the beginning of the algorithm [26].
After subtracting the background, the experimental data needs to be fitted with an appropriate function to identify the peaks corresponding to the different chemical states of the materials. In this study, the Voigt profile probability distribution will be used, which is defined as the convolution of a Cauchy-Lorentz distribution and a

Gaussian distribution [27]. Mathematically, the Voigt profile is described by the following equation [27]:

$$V(x;\ \sigma,\gamma) \equiv \int_{-\infty}^{\infty} G(x';\sigma)\ L(x-x';\gamma)\ dx'$$

$$G(x;\sigma) = \frac{1}{\sqrt{2\pi}\sigma} e^{-\frac{x^2}{2\sigma^2}} \qquad (3.2)$$

$$L(x;\gamma) = \frac{\gamma}{\pi(x^2+y^2)}$$

where $G(x;\sigma)$ is the centered Gaussian and $L(x;\gamma)$ is the centered Lorentzian profile. The broadening of the spectrum due to Gaussian distribution is caused by the uncertainty in the equipment, whereas the Lorentzian broadening is due to the lifetime of the photoelectrons. For the peak fitting, KolXPD software is used. For the data processing, Origin software (2023b) and MATLAB computing platform were used.

As mentioned earlier, the STM setup (provided by SPECS Surface Nano Analysis, GmbH) is connected to the NAP-XPS system, and the sample can be transferred to the STM chamber under UHV conditions without being exposed to open air. This allows for a reliable observation of the morphology of the sample before or after XPS measurement. The pressure in the STM chamber was 1×10^{-10} mbar. The STM scans were obtained using a so-called KolibriSensor (nc-AFM/STM sensor). The voltages used for the sample were between 2.5 - 4.0 V (depending on the thickness of the prepared layer). The adjusted measurement mode for the acquired figures was the constant current mode.

4. Experimental results

The goal of the experiment is to obtain a comprehensive understanding of the interaction between epitaxial stoichiometric $CeO_2(111)$ layers with water vapor under operando conditions. We have prepared three different types of $CeO_2(111)$ layers on a Pt(111) single crystal. The samples were prepared based on experimental procedures of $CeO_2(111)$ preparation on Cu(111) with controlled density of steps – theory and methods developed by F. Dvořák et al. [28] and T. Duchoň et al. [29]. The growth of controlled density of steps relies on the self-arrangement properties of cerium and oxygen which depend on the careful control of deposition parameters (for example changes in sample temperature or oxygen background pressure during the cerium deposition). The prepared layers are henceforth referred to as the $CeO_2(111)$ classical layer (grown at a certain temperature in a classical way), the gradual layer (grown under a gradual temperature gradient), and the the redox layer (based on a gradual layer with the further reduced-oxidized process), depending on its preparation procedure. For every prepared $CeO_2(111)$ layer, the morphology of the surface was observed by STM, and the density of steps was calculated according to the procedure explained previously by F. Dvořák et al. [30]. XPS was carried out to obtain information about layer thickness and CeO_2 stoichiometry, followed by further confirmation of the surface crystalline structure by LEED.

After obtaining the necessary information about each prepared layer, samples were further loaded in the NAP cell to initiate the primary phase of the experiment, which involved investigating the interaction between the prepared $CeO_2(111)$ layer and water vapor under different pressures. This was accomplished by conducting an isotherm reaction utilizing water vapor. The water vapor pressure within the cell was gradually increased while the sample was maintained at ambient temperature. XPS spectra were collected at each step of the water vapor pressure. The procedure was repeated for all three layer models: classical, gradual, and redox layers.

4.1 Layer preparation

4.1.1 Cleaning procedure for Pt(111) single crystal

For all experiments, we used a hat-shaped Pt(111) single crystal (MaTeck, GmbH) as substrate, with purity 99.9999%, roughness below 0.01 μm, and orientation accuracy below 0.1°. Layer preparation was the very first and most important step in the experiment setup. Every layer preparation began with cleaning the Pt(111) single crystal. The standard cleaning process involved argon ion sputtering of the as-received Pt(111) single crystal at room temperature with an argon pressure of 5×10^{-6} mbar for 30-60 minutes. The length of the sputtering depended on the extent of the contamination. If the single crystal was not used for a long time, strong bonds of Pt-C could be formed on the single crystal surface, which would require a longer sputtering process. Caution must be exercised with longer argon ions sputtering, as leaving the sample to be sputtered for too long can result in damage to the single crystal. To avoid this, the whole cleaning process was repeated as many times as necessary. After the argon sputtering, the argon was allowed to be evacuated and replaced with oxygen molecules. Once the pressure had stabilized at 5×10^{-7} mbar, the sample temperature was increased until it reached the range of 855 K - 875 K, where it was kept for one minute for annealing. The sample was then cooled down to room temperature and the oxygen was evacuated. This part of the cleaning process is known as annealing in O_2 and its main purpose is to burn any possible carbon contamination species on the surface. The last step involved flashing the sample at higher temperature in UHV conditions. The temperature was raised to 925 K and immediately cooled down to room temperature. The cleaning process is illustrated in Figure 4.1.

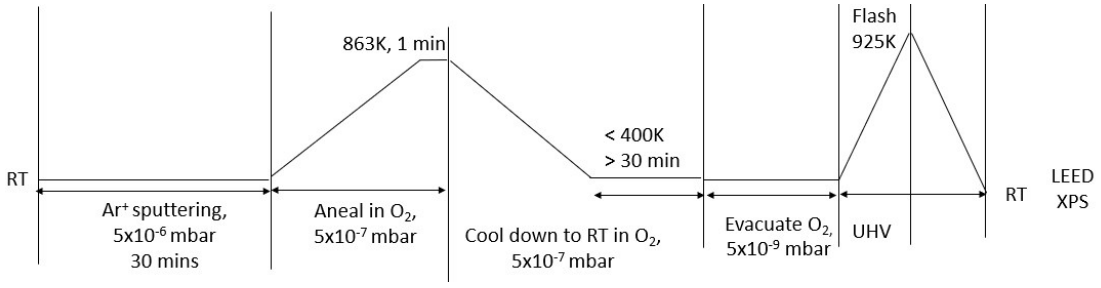

Figure 4.1: Illustration of one cleaning cycle of the Pt(111) single crystal.

After the cleaning process, LEED was applied to verify the Pt(111) orientation and confirm the cleanliness of the Pt(111) surface. The resulting image, shown in Figure 4.2, exhibited a hexagonal symmetry with bright and sharp spots. The distance between the spots, as well as the sharpness, brightness, and symmetry, confirmed the presence of the desired Pt(111) structure. This provided a confirmation that the surface was clean and well-defined.

The chemical composition of the surface was analyzed using XPS, and the results are displayed in Figure 4.3. Figure 4.3 a) shows the survey spectrum covering a binding energy range of 0 - 1100 eV. Core level spectra were further carried out after survey spectrum. In this case, the core level spectra of Ce 3*d*, O 1*s* + Pt 4$p_{3/2}$, Pt 4*f,* and C 1*s* were measured. Measuring the Ce 3*d* level is necessary to check the residual of CeO_2 and confirm a baseline of clean samples. The result in Figure 4.3 e) indicates that there is no cerium species present on the surface. Additionally, the most important experiment in the thesis focuses on changes in the O 1*s* + Pt 4$p_{3/2}$ core level spectra, and a core-level spectrum of O 1*s* + Pt 4$p_{3/2}$ from a clean sample was conducted for comparison (Figure 4.3 d)). Generally, it is very difficult to completely get rid of carbon contamination in the chamber, and carbon is likely to react with Pt(111) single crystals. Thus, C 1*s* spectra were closely monitored during each step of the XPS measurement (Figure 4.3 b)). The Pt 4*f* level peak has the highest intensity of platinum, and its attenuated intensity after CeO_2 preparation will be used for calculating the thickness of the CeO_2 layer (Figure 4.3 a)).

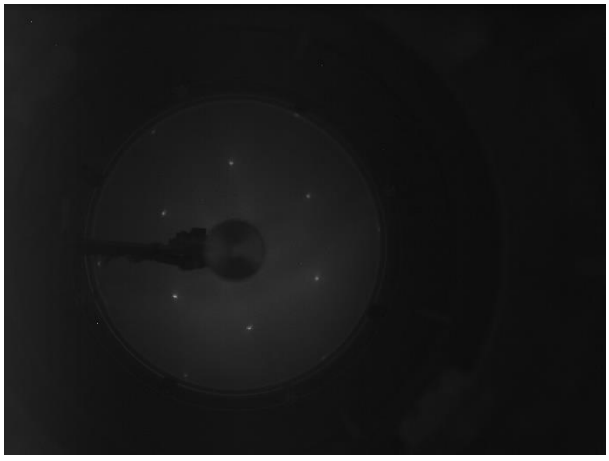

Figure 4.2: LEED image of clean Pt(111) single crystal.

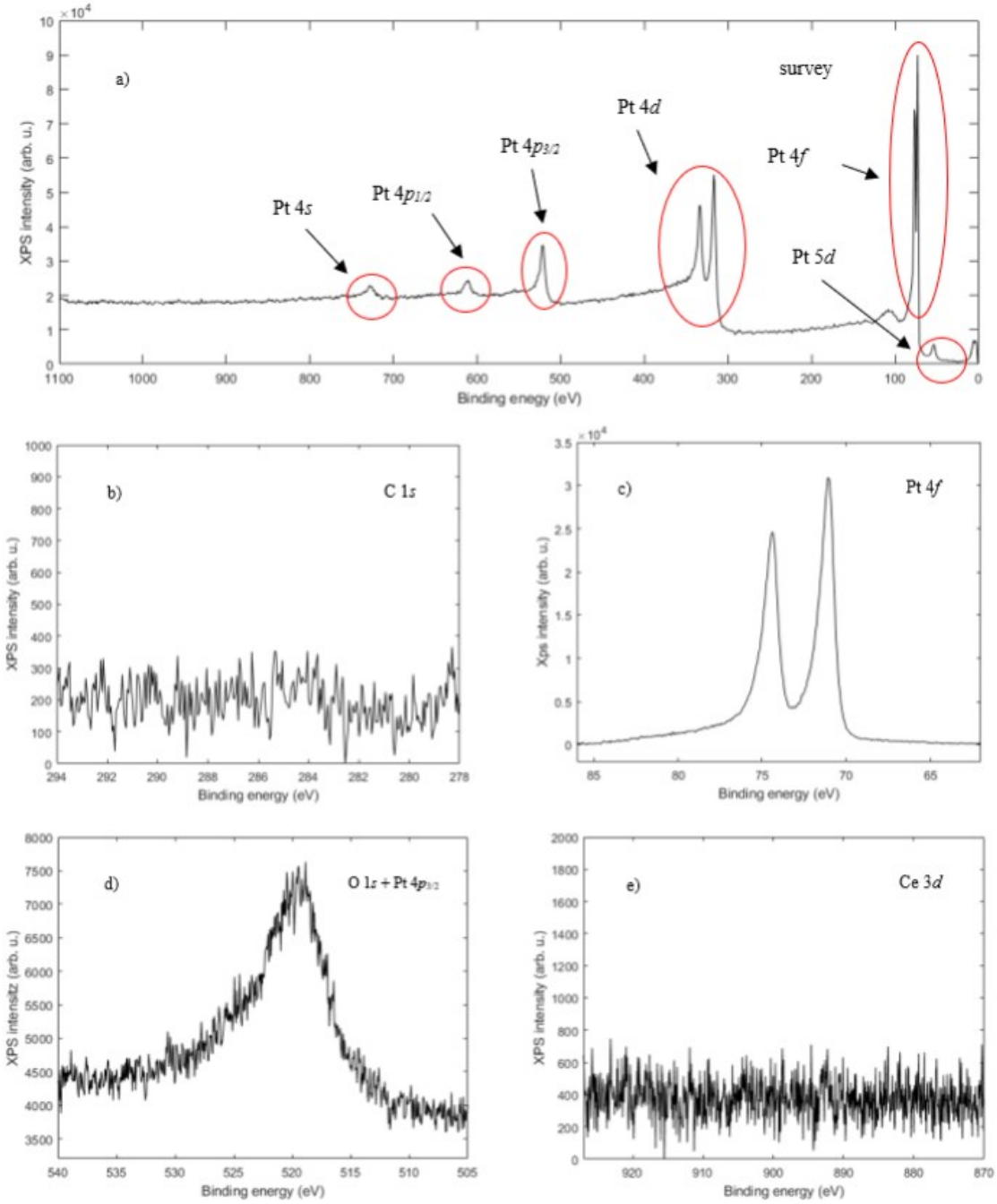

Figure 4.3: XPS scan of clean Pt(111) single crystal.

4.1.2 Preparation of CeO_2(111) classical layer on Pt(111)

After the cleaning procedure, the epitaxial stochiometric CeO_2 layer was grown on the Pt(111) single crystal by depositing cerium atoms from an overheated cerium rod in an O_2 background. Ce (Goodfellow, 99.9%) was evaporated from a molybdenum crucible heated by an electron beam. The classical growing process was carried out at 523 K, by heating up the Pt(111) single crystal in an ultra-high vacuum before layer growth. Once the temperature had stabilized, the preparation chamber was filled with 5×10^{-7} mbar O_2, and the Ce evaporation was started. The Ce deposition in an O_2 background lasted for 150 minutes while we attempted to maintain the sample temperature as stably as possible. The deposition time was chosen according to the desired layer thickness. The deposition speed (monolayer per minutes) was estimated from the layer growth of a previous experiment. It was assumed that the layer grew linearly over time. According to T. Duchoň et al. [29], it is not possible to prepare a thin layer from the system called redox layer (will be described later in the thesis) so the deposition time was adjusted to get a comparable CeO_2 thickness for all the three systems prepared for the experiment.

The sample was then annealed in the oxygen background, by heating up to 725 K and immediately cooling it down. The annealing step is an important step to ensure the mobility of oxygen atoms and achieve a stoichiometric Ce^{4+} layer. During the annealing, slow heating and cooling of the sample were necessary to avoid cracking the grown CeO_2 layer. After the sample temperature dropped below 400 K, the oxygen was evacuated by the pumping system, and the layer was prepared for characterization. The graphical illustration of the process is represented in Figure 4.4.

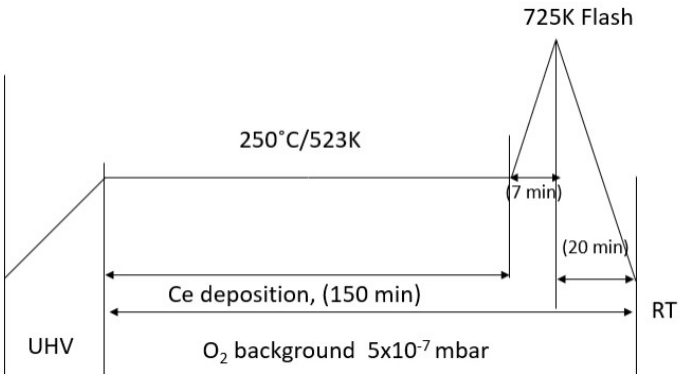

Figure 4.4: The growth procedure of the classical layer.

After the preparation of the layer, the sample was further characterized by STM, LEED, and XPS. These techniques provided us with valuable information regarding the surface morphology, crystal structure, and chemical composition of the prepared layers.

Figure 4.5 shows the STM image obtained from the prepared $CeO_2(111)$ classical layer.

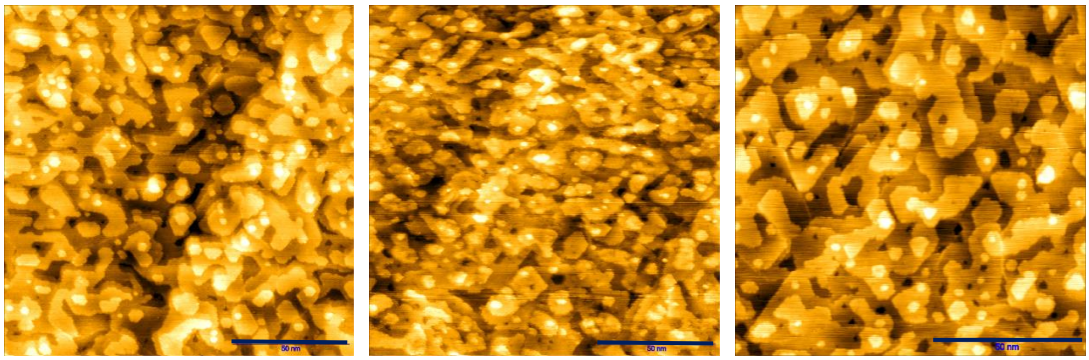

Figure 4.5: The STM images of the $CeO_2(111)$ classical layer.

The figure shows three images with a 50 nm scale. The different colors on the map represent different outbursts from the surface, with consistent sets of one-color representing ceria islands. The boundaries of these islands illustrate the step edges.

In Figure 4.6, the calculation of density of step edges from the masked STM image is illustrated, along with partial results of the calculation. The step-edge density calculations indicated the density of step edges is around 10.5% for the prepared $CeO_2(111)$ classical layer.

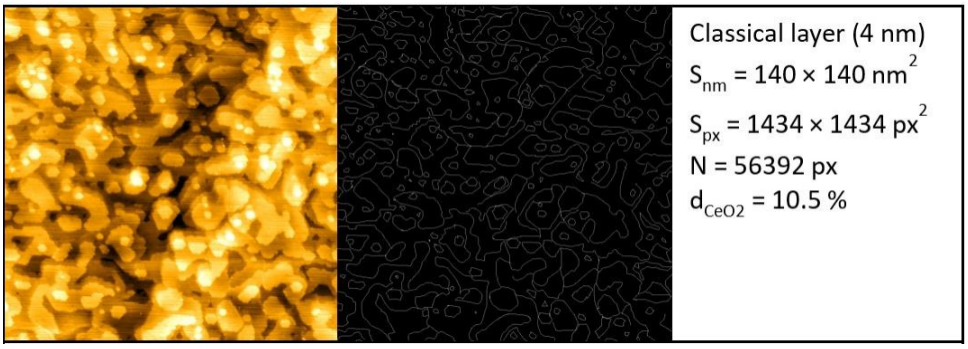

Figure 4.6: Step edge density calculation example for the classical layer.

The height profile is shown in Figure 4.7. It is obtained from STM images, where the height of the surface terraces is coded into the colormap – the lighter is the color, the higher is the observed point in the surface. The height profile in Figure 4.7 shows that there were 3 to 4 monolayers that remained exposed, with terrace dimensions measuring less than 10 nm.

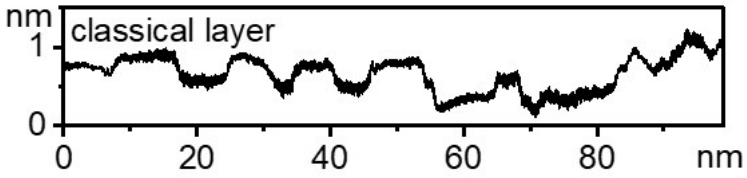

Figure 4.7: The STM height profile of the classical layer.

To check if the required CeO_2(111) structure was present on the surface after layer deposition, LEED was performed, and the results can be found in Figure 4.8.

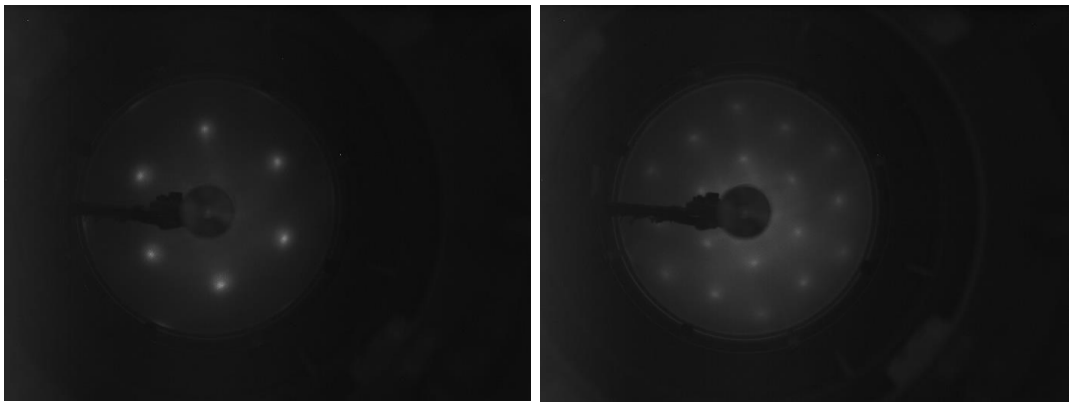

Figure 4.8: The LEED patterns of the classical CeO_2(111) layer (two different patterns are illustrated with different electron energy, following in order 60 eV and 130 eV).

LEED image shows obscure, slightly blurred spots arranged in a hexagonal form, which is typical for surface structures of a (111) lattice type. The 60 eV pattern shows the very top part of the layer, while the 130 eV scan gives insight into the lower levels, as well. Thus, the LEED pattern suggests a successful preparation of the CeO_2(111) layer. The blurriness suggests a less continuous surface with smaller ceria islands and

a significant amount of step edges. No visible spots of Pt(111) also ensures the continuity of the prepared CeO_2(111) layer.

The XPS spectra of the prepared layer was also measured. Since the XPS spectra of the cleaned Pt(111) surface was measured, the thickness of the CeO_2 layer was estimated from the intensity of the main Pt 4*f* peaks before and after the deposition using the equation below:

$$d = \lambda \ln\left(\frac{I_0}{I_d}\right), \qquad (4.1)$$

where d denotes the layer thickness, λ is a so-called inelastic mean free path (IMFP), constant with a value of *22.34 Å* for Pt 4*f*, I_0 is the intensity of the Pt $4f_{7/2}$ peak before the layer deposition and I_d is the intensity of the same peak after the layer deposition.

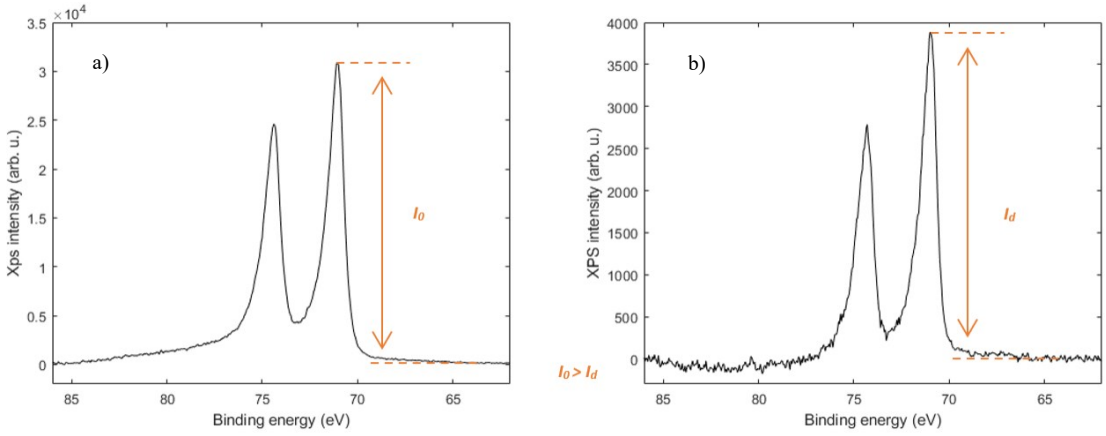

Figure 4.9: The Pt 4*f* core level spectra of (a) clean Pt(111) surface and (b) deposited CeO_2(111) layer on Pt(111) surface.

The estimated layer thickness for the classical layer, calculated by using the equation (4.1) is *42.1 Å*, which is *13.6 monolayer*. (In the case of CeO_2(111), a monolayer corresponds to a distance of 3.12 Å [31]).

The XPS spectra in Figure 4.10 provide information about the chemical composition of the prepared surface. The CeO_2 layer on the Pt(111) surface is visible with intense CeO_2 peaks in the Ce 3*d* region (binding energy at 917-880 eV) and the O 1*s* region (around 530 eV). The Pt 4*f* peak shows a significant decrease in intensity due to the

presence of the thick cerium oxide layer (the signal is attenuated). Additionally, a small peak is visible around 290 eV identified as a Ce 1*s* peak, indicating the presence of ceria.

In subfigure 4.10 e), the fitted peaks of the Ce 3*d* region are illustrated. Five doublets are distinguishable. Three doublets of Voigt function (as described in the experimental setup part of the thesis regarding data analysis) were identified as Ce^{4+}, and two doublets with main peak energies of 880.8 eV and 885.8 eV were identified assigning to Ce^{3+} [16].

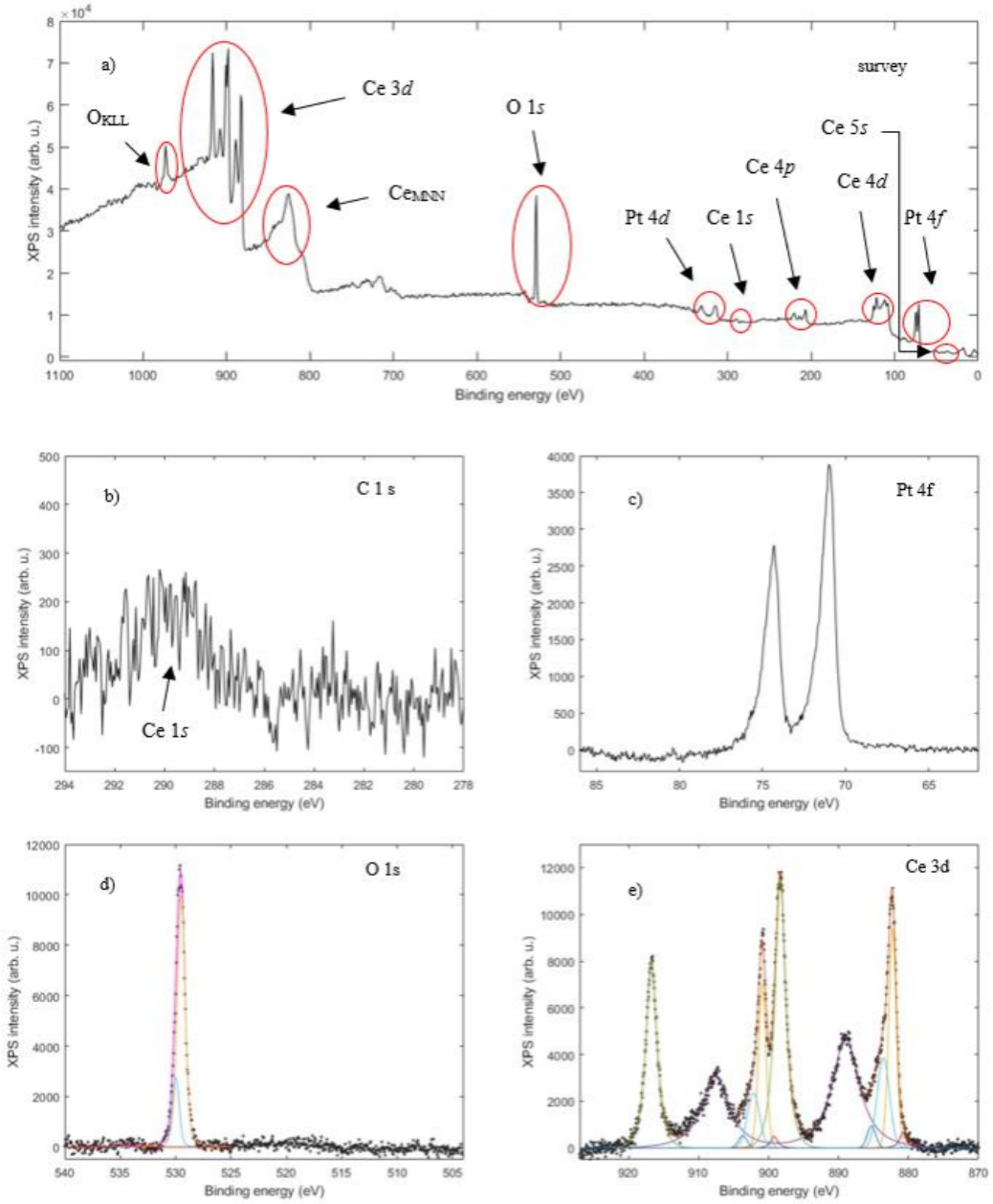

Figure 4.10: The XPS spectra of the classical CeO_2(111) layer

The orange and light blue peak physically represents one widened, asymmetrical peak with main peak energy of 882.3 eV (representing one of the Ce^{4+} peaks). The peak can be fitted as a sum of two theoretical Voigt functions [16] with different relative intensities, slightly different main energies, and widths. In the forthcoming parts of the thesis, the sum of these two theoretical peaks will be depicted for each Ce 3*d* graph, as a singular Ce^{4+} doublet.

4.1.3 Preparation of CeO_2(111) gradual layer on Pt(111)

Before depositing cerium oxide for our gradual layer, the platinum single crystal was cleaned using the previously described method. Pt 4*f* reference core-level spectrum was then measured for layer thickness calculations later, and the cleanliness of the single crystal was also confirmed as described previously.

The illustration of the deposition process of CeO_2(111) gradual layer is represented in Figure 4.11.

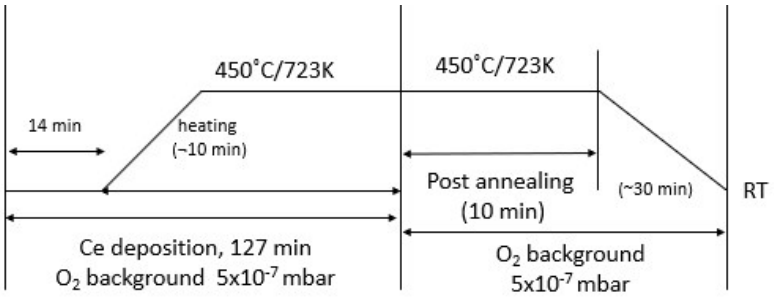

Figure 4.11: The CeO_2 deposition process for the gradual layer.

The Ce deposition began in a background of 5×10^{-7} mbar O_2 at room temperature (RT). After 14 minutes of deposition at RT, which corresponds to the formation of 1.5 monolayers (buffer layer), calculated from the measured speed of the cerium oxide deposition; the adjacent layers subsequently grow epitaxially on top of the buffer layer, the sample was gradually heated under O_2 atmosphere to 723 K, which took 10 minutes to reach the final temperature. After 127 minutes, the cerium deposition was switched

off, and the sample was post-annealed in the same oxygen background. The ensuing cooling process, which lasted until the sample reached room temperature took 30 minutes.

To avoid layer cracking, the sample temperature had to be changed slowly. However, if the sample stays in the preparation chamber for a couple of hours, some carbon contamination could appear. To clean the contamination, a so-called "layer refreshing" method was used (Figure 4.12) when prepared layer was kept for longer time (typically overnight) in the preparation chamber.

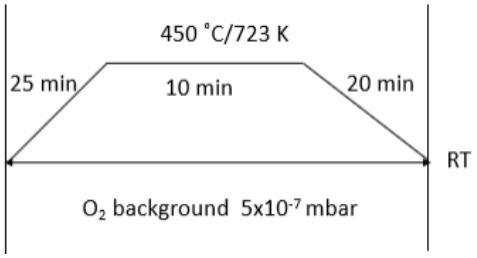

Figure 4.12: The procedure of CeO_2(111) layer refreshing.

The refreshing process involves slow heating of the sample to 723 K, keeping it at this temperature, and then slowly cooling it down to room temperature, all in an oxygen background with a pressure of 5×10^{-7} mbar. The heating and cooling process should be slow (with a gradient of approximately 1 K per 1 s), otherwise, the CeO_2 layer could crack due to the fact that the two different layers have different reactions to heat, and CeO_2 accommodates slower to temperature changes than the metal platinum. After this procedure, the carbon contamination disappeared as a consequence of two effects: firstly, due to the increased thermal energy, the carbon desorbs from the surface; secondly, if the temperature is high enough, the desorbed carbon reacts chemically with the oxygen molecules, forming carbon dioxide. Thus, the contamination is eliminated.

For the layer characterization XPS, LEED and STM were measured. The CeO_2 layer thickness was calculated based on the attenuation of Pt 4*f* core level spectra by equation (4.1). The estimated layer thickness for the gradual layer, calculated by using the equation (4.1) is *37.6 Å,* which corresponds to *12.1 monolayer*.

The STM images of the CeO_2(111) gradual layer are represented in Figure 4.13.

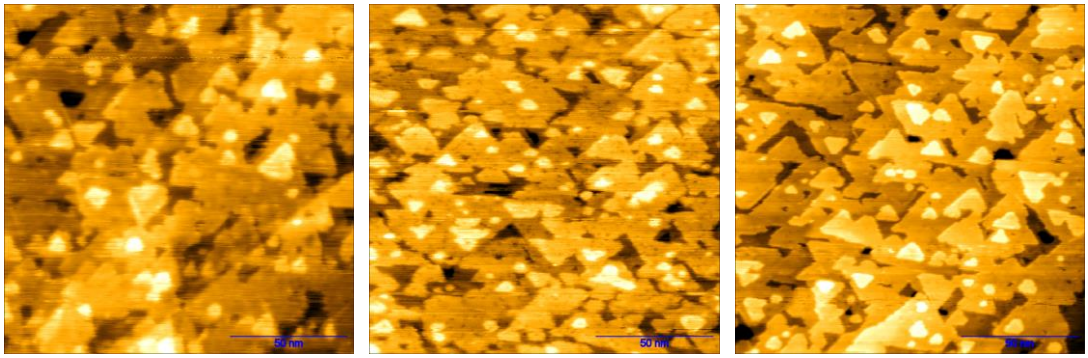

Figure 4.13: The STM images of the prepared CeO_2(111) gradual layer.

The height profile of the gradual layer is illustrated in Figure 4.14. It shows that the layer has 2 - 3 monolayer openings with terrace sizes approximately 15 nm. The step edge percentage calculation shows *8%* for the prepared gradual layer.

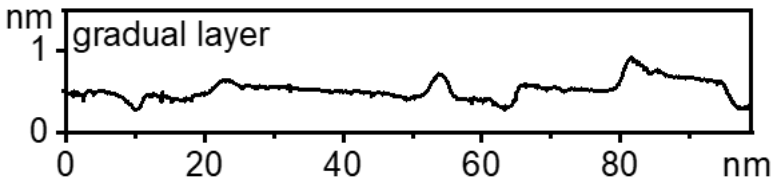

Figure 4.14: Height profile of the prepared CeO_2(111) gradual layer.

The LEED pattern of the layer was also observed to assess the surface morphology. The results are depicted in Figure 4.15.

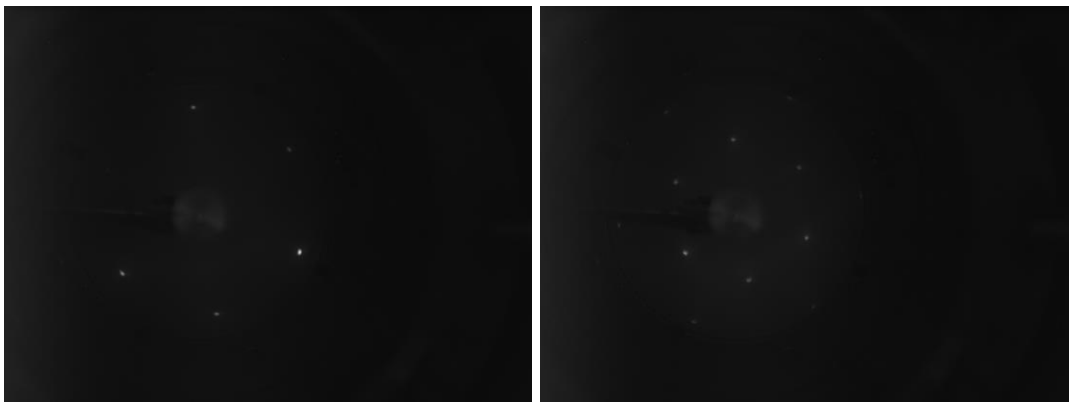

Figure 4.15: The LEED pattern of the gradual CeO_2(111) layer (two different patterns are illustrated with different electron energy, following in order 60 eV and 130 eV).

In Figure 4.16, the measured XPS spectra are shown in the following order: a) survey scan, b) C 1*s*, c) Pt 4*f*, d) O 1*s*, and e) Ce 3*d* core level spectra.

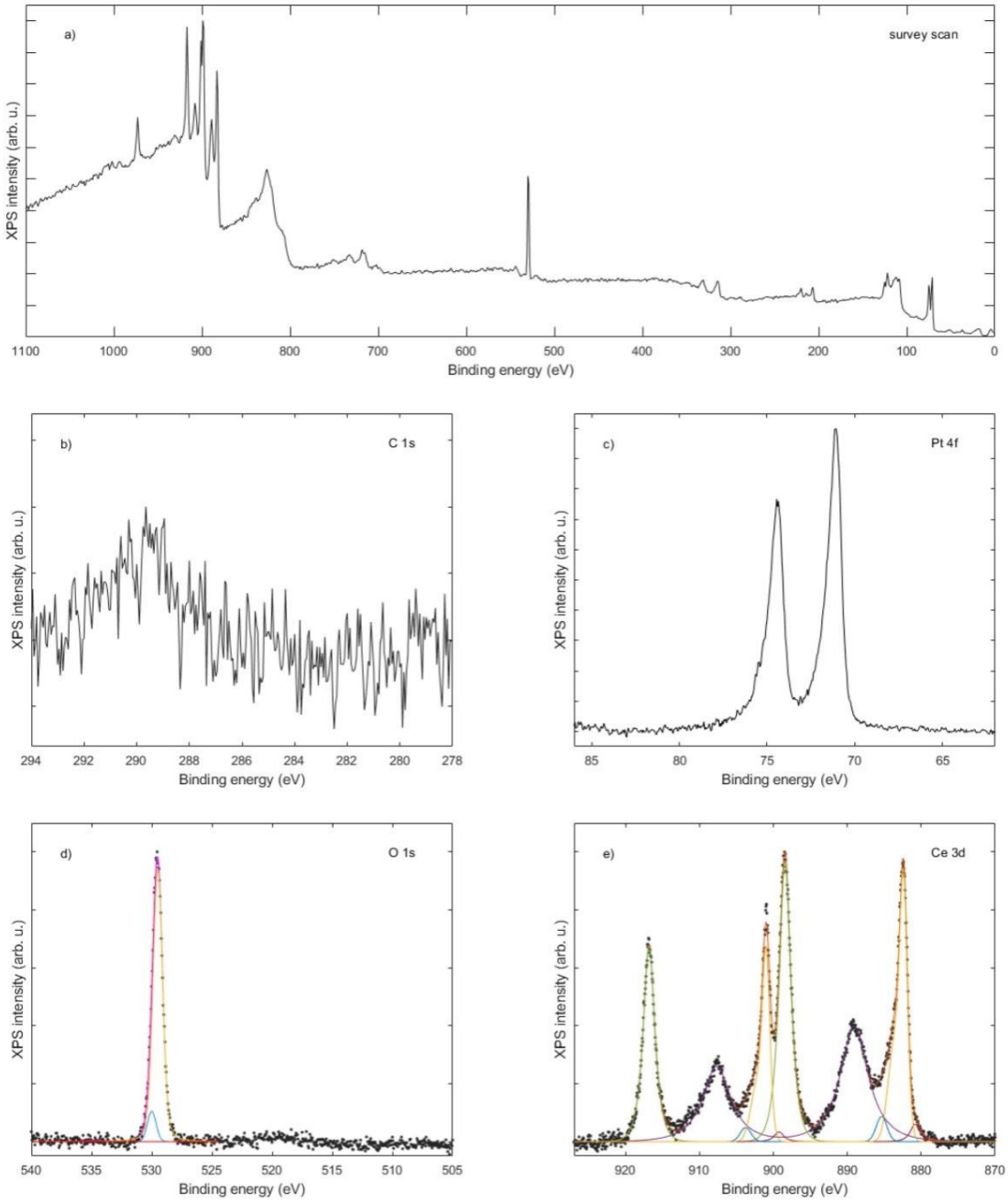

Figure 4.16: The XPS spectra of the prepared CeO_2(111) gradual layer.

4.1.4 Preparation of CeO_2(111) redox layer on Pt(111)

The layer preparation steps were carried out according to the reported experiments by T. Duchoň et al. [29] with slight modifications and using Pt(111) single crystal as substrate.

The first step of the redox CeO_2(111) layer deposition procedure was to grow an oxidized buffer layer following the same procedure for gradual layer deposition. The preparation chamber was filled with 5×10^{-7} mbar oxygen, and the deposition of Ce started at room temperature. After 1.5 monolayer deposition, the deposition was carried out in a gradual heating process up to 723 K. The Ce deposition lasted 29 minutes in total, and the prepared layer was post-annealed in oxygen background for 10 minutes. The process is illustrated in Figure 4.17.

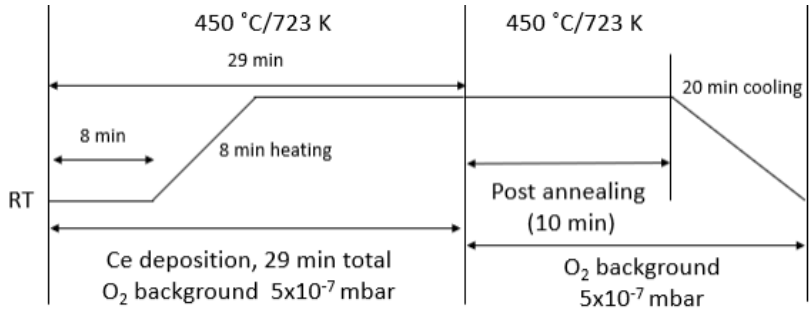

Figure 4.17: Oxidized CeO_2(111) buffer layer deposition similar to a gradual layer, a prior step for the redox layer growth.

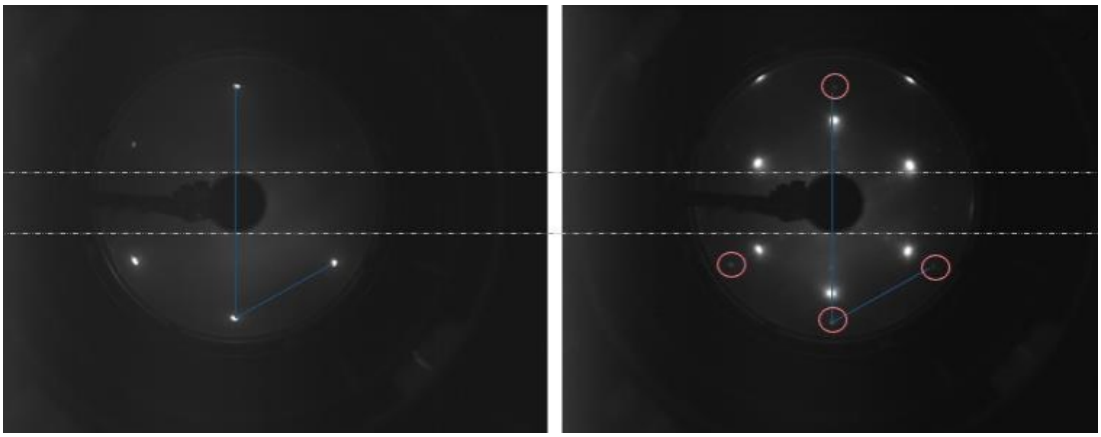

Figure 4.18: Pt(111) and the buffer layer after the first CeO_2 deposition LEED patterns.

LEED was used to verify the continuity of the layer (Figure 4.18). After the deposition, Pt(111) spots (highlighted with red circles) were still observable, but CeO_2 structure spots were also present. It was decided to continue the growth with more CeO_2 deposition. The sample was then heated up to 723 K in an O_2 background and Ce were deposited for 16 minutes.

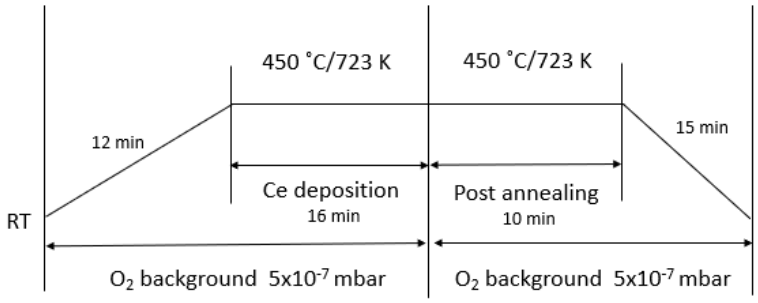

Figure 4.19: Second CeO_2 deposition on the buffer layer.

As demonstrated in Figure 4.20, residual Pt(111) spots are perceptible on the surface, albeit significantly fainter.

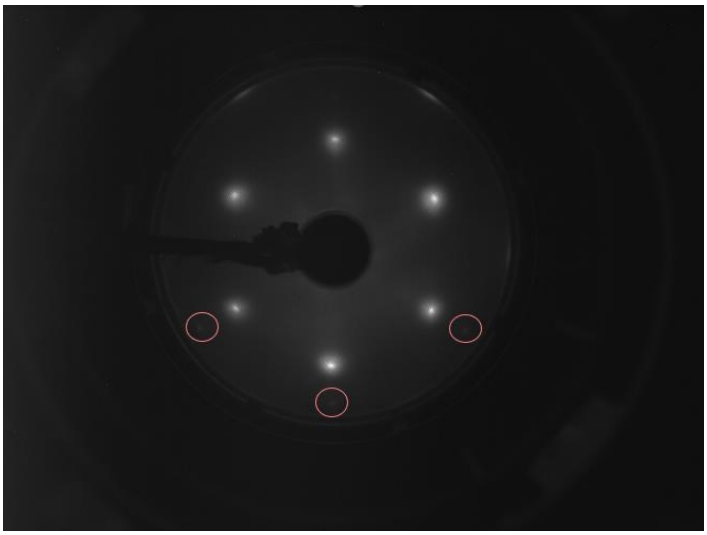

Figure 4.20: The buffer layer after the second CeO_2 deposition.

One more deposition cycle was performed due to the residual platinum spots, as illustrated in Figure 4.21. After the third deposition, no Pt(111) spots were observed

on the LEED image, and therefore the reduction procedure of the buffer layer could be started.

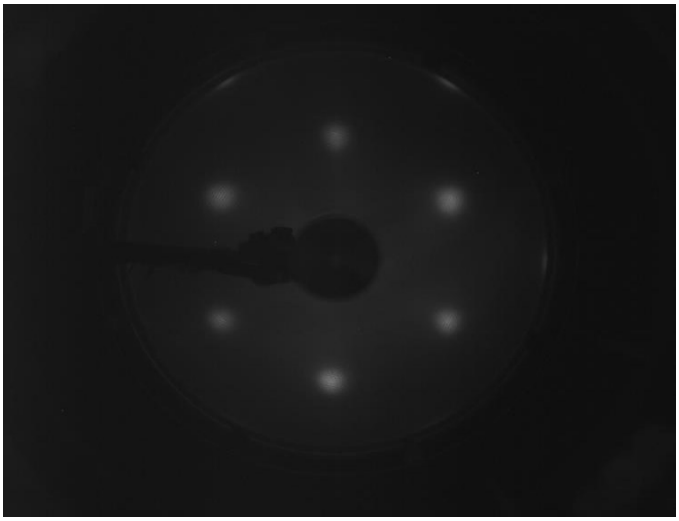

Figure 4.21: The buffer layer after buffer CeO_2(111) deposition – no Pt(111) spots were observable.

The reduction is composed of Ce deposition at room temperature for 70 minutes under UHV conditions and followed by annealing the sample at 900 K in UHV for 30 minutes [29]. The procedure is illustrated in Figure 4.22. After the reduction, the prepared CeO_2(111) was reduced to CeO_x(111) with x at approximately 1.8 confirmed by XPS.

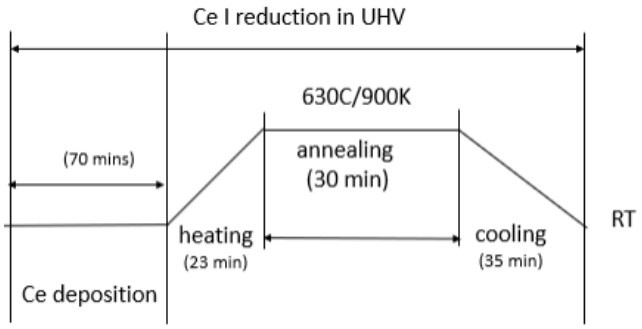

Figure 4.22: Reduction of the buffer layer.

After the reduction, the oxidation process started at room temperature with an oxygen background of 5×10^{-8} mbar. After 10 minutes, the sample was heated until it reached

400 K and was kept at that temperature. Then, after 20 minutes, the oxygen pressure in the preparation chamber was increased to 5×10^{-7} mbar. After 10 minutes of oxygen deposition, the sample was heated up to 500 K. After a further 20 minutes, the oxygen pressure was again increased, precisely to 5×10^{-6} mbar, and kept at the same conditions for 50 minutes. The total oxygen exposure reached 5850 L (1 L – Langmuir – corresponds to an exposure of 10^{-6} Torr, which is approximately 1.33×10^{-6} mbar, during one second).

For the last steps, the layer was refreshed by oxygen annealing at 723 K, reduced by annealing in UHV at 900 K, and annealed again in oxygen background at 723 K. The steps of the process are illustrated in Figure 4.23.

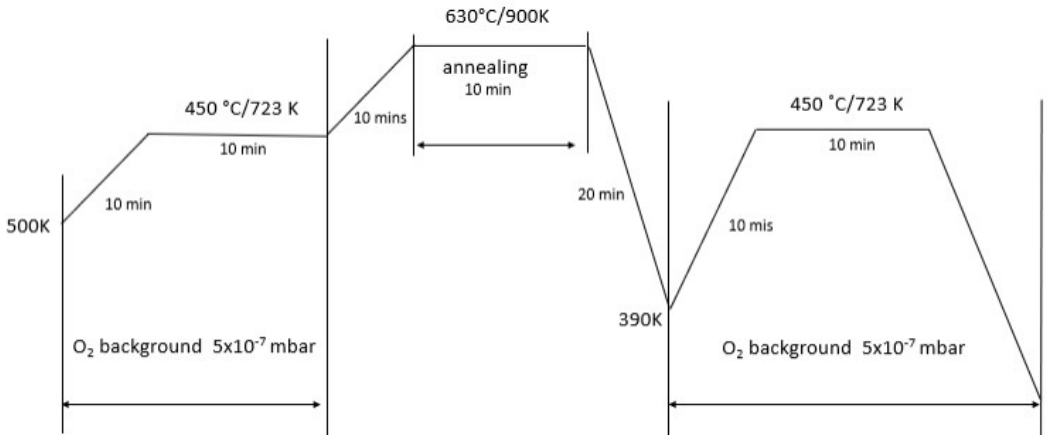

Figure 4.23: Final steps of the preparation of our redox layer

For the layer characterization the STM, LEED and XPS data of the sample was measured. The STM scan of the surface is illustrated in Figure 4.24.

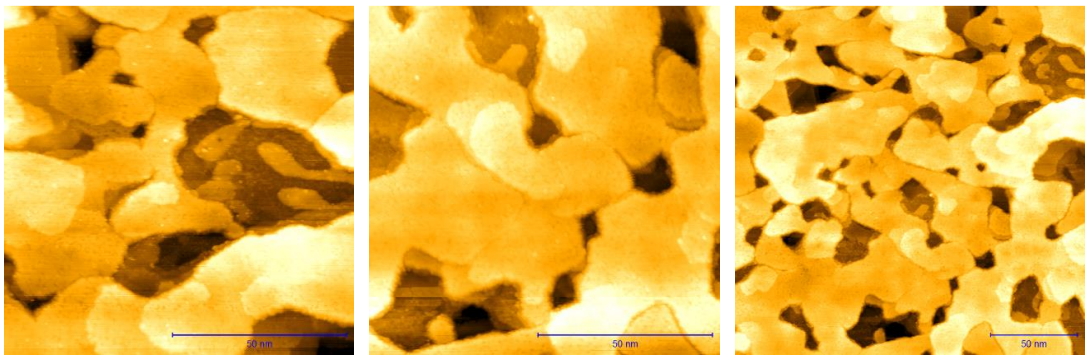

Figure 4.24: The STM figures of the redox layer.

In Figure 4.25 the height profile of the sample is presented. The step edges calculation gave value of *5.7%.*

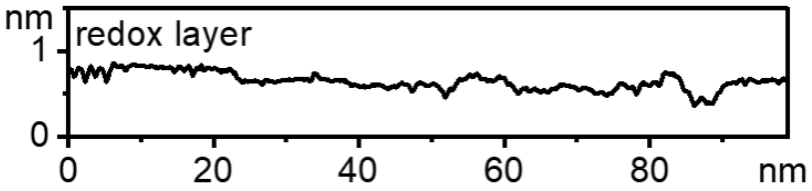

Figure 4.25: Height profile of the redox layer.

LEED (Figure 4.26) shows the LEED pattern of prepared redox layer with a CeO_2(111) structure.

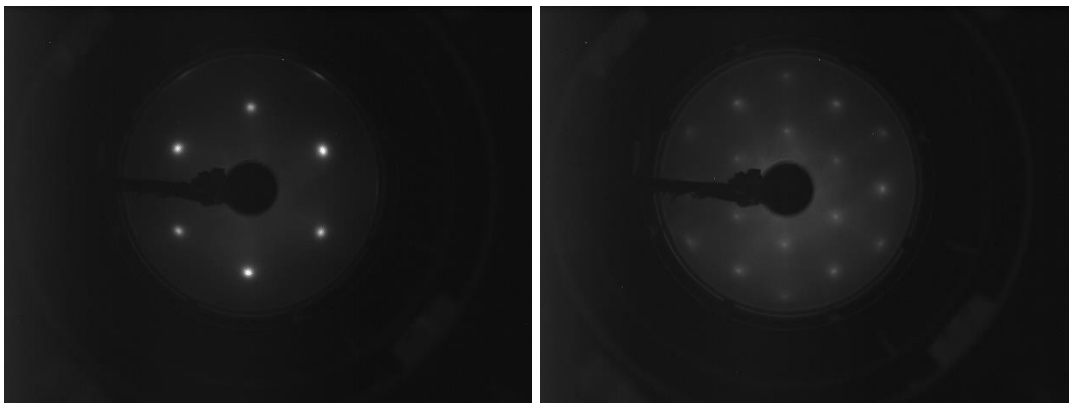

Figure 4.26: The LEED patterns of the redox CeO_2(111) layer (following in order 60 eV and 130 eV).

The XPS spectra are shown in Figure 4.27. The layer thickness was then calculated using equation (4.1) and found to be *49.0 Å*, which corresponds to *15.8 monolayers*.

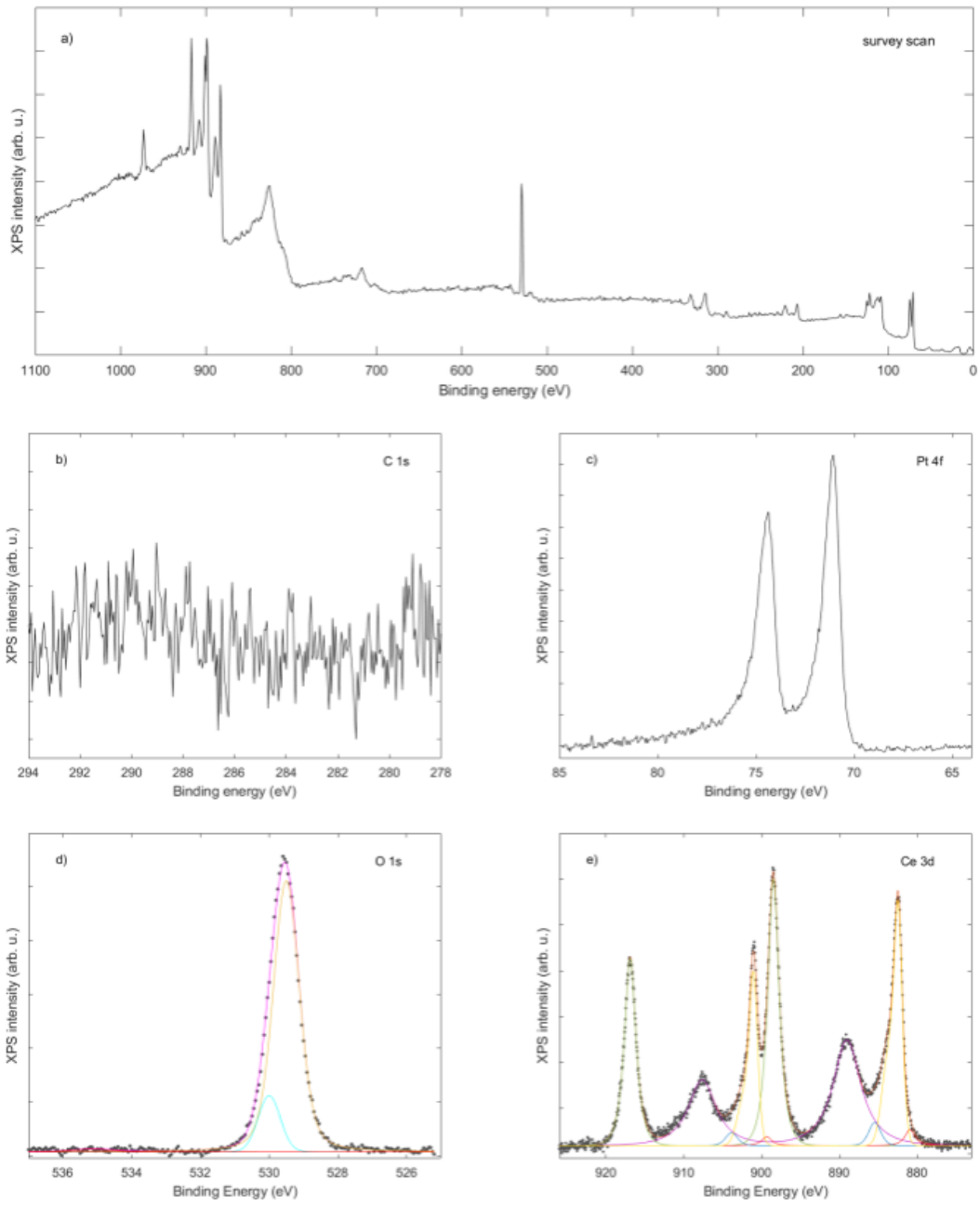

Figure 4.27: The XPS spectra of the $CeO_2(111)$ redox layer.

4.2. Water interaction of three prepared CeO_2(111) layers

4.2.1 Experimental preparation, the cleaning procedure

Before each experiment, it is necessary to decontaminate the environment where the experiment is carried out as much as possible, as well as to clean the sample itself. In our case, it is important to ensure that the NAP cell, the sample, the water doser (which is used to introduce clean water vapor into the cell), and the lines through which the vapor is led into the NAP cell are all clean.

For our experiments, very clean and pure water is required. For the preparation of clean water with resistivity 18.2 MΩ·cm @ 25 °C, a Milli-Q® Type 1 ultrapure water system (Millipore, Merck) was used. The whole water doser (which is installed afterward in the measurement setup) is filled and sonicated for at least five minutes. The metal parts of the tube are washed at least 3-5 times with fresh ultrapure water as well. After repeating the wash-out process 2-3 times, the container was filled with fresh water for the experiment. During the entire preparation process, contact with plastic containers and water is avoided.

After the installation of the water dozer on the experimental setup, it was purified with 5 freeze–pump-thaw cycles before usage.

The NAP cell cleaning process begins with flushing the cell with oxygen at pressure around 2 mbar and stage temperature approximately 700 K for 8 hours followed by 6 - 7 hours of H_2O flushing at 1 mbar at room temperature (typically overnight). After the H_2O is switched off, the cell is heated up to 700 K (stage temperature) at approximately 2 mbar O_2 for 1 hour. The cell is cooled down in oxygen. After the cleaning process, the cell partial pressures are checked with QMS, and the following work begins when the H_2O partial pressure drops down below 10^{-13} A in the QMS signal.

Clean CeO_2 on Pt(111) sample is transferred inside the NAP cell, and the XPS spectrum is firstly measured under UHV conditions. If the sample is considered clean, the water interaction with cerium oxide CeO_2(111) experiment can be started.

4.2.2 Experimental results and discussion

Before transferring the sample into the NAP cell, two XPS scans were taken - one at 0° and 70° rotation - to confirm the absence of any carbon contamination on the surface. The 70° rotation provides a different perspective and has a smaller information depth, making the eventual contamination peak relatively more intense compared to the CeO_2(111)/Pt(111). If no contamination peak is observed from both angles, the surface is considered sufficiently clean for the experiments.

During the experiment, the interaction of water vapor with ceria was observed at isothermal conditions, with gradually increasing water vapor pressure in the NAP cell while keeping a constant temperature. The QMS signal was collected during the whole experiment to control the partial pressure of gas outlet in the cell, which is useful for detecting any contamination that could compromise the experiment's accuracy.
To minimize the impact of X-ray exposure on the sample's surface, the smallest measurement spot was selected, and the radiated spot was changed for each new measurement after the pressure adjustments. It is assumed that the sample has a homogeneous surface, including the step edges and the amount of ceria.

The experimental steps for the classical layer are shown in Table 1, the gradual layer in Table 2, and for the redox layer in Table 3. The tables contain the technical details of the experiment, in order: the number of the measurement step, the sample temperature during the associated measurement step, the theoretically planned pressure condition, the NAP cell pressure, the NAP lens pressure (measured in the first pumping stage right behind the nozzle, see Figure 3.3 on page 17), and the QMS partial pressure for H_2O including the fluctuation range, and the exposure time under X-ray for each measured spot.

Table 1

No.	Sample temperature	Target pressure	NAP cell pressure (mbar)	NAP lens pressure (mbar)	QMS 18 AMU – H_2O (A)	X-ray exposure time
1	307 K	UHV	N/A	2.9×10^{-9}	8.50×10^{-14}	~ 43 min
2	306 K	10^{-3} mbar	N/A	$(2.90\text{-}3.13)\times10^{-8}$	$(3.50\text{-}3.43)\times10^{-12}$	~29 min, dif. spot
3	304 K	0.01 mbar	N/A	$(2.17\text{-}2.26)\times10^{-7}$	$(3.63\text{-}3.45)\times10^{-11}$	~29 mins, dif. spot
4	303 K	0.05 mbar	$(4.07\text{-}4.07)\times10^{-2}$	$(4.16\text{-}4.26)\times10^{-7}$	$(6.30\text{- }6.23)\times10^{-11}$	~29 mins, dif. spot
5	302 K	0.10 mbar	$(1.02\text{-}0.98)\times10^{-1}$	$(9.13\text{-}9.30)\times10^{-7}$	$(1.44\text{-}1.46)\times10^{-10}$	~29 mins, dif. spot
6	301 K	0.15 mbar	$(1.46\text{-}1.51)\times10^{-1}$	$(1.27\text{-}1.29)\times10^{-6}$	$(2.09\text{-}2.10)\times10^{-10}$	~29 mins, dif. spot
7	301 K	0.20 mbar	$(1.99\text{-}1.99)\times10^{-1}$	$(1.74\text{-}1.75)\times10^{-6}$	$(2.94\text{-}2.9)\times10^{-10}$	~29 mins, dif. spot
8	301 K	0.4 mbar	$(4.03\text{- }3.95)\times10^{-1}$	$(3.62\text{-}3.59)\times10^{-6}$	$(6.53\text{-}6.46)\times10^{-10}$	~35 mins, dif. Spot
9	300 K	1 mbar	$(1.01\text{-}0.93)\times10^{-1}$	$(1.07\text{-}1.01)\times10^{-5}$	$(1.54\text{-}1.48)\times10^{-9}$	~42 mins, dif. spot

Table 2.

No.	Sample temperature	Target pressure	NAP cell pressure (mbar)	NAP lens pressure (mbar)	QMS 18 AMU – H_2O (A)	X-ray exposure time
1	344 K	UHV (NAP cell)	N/A	2.33×10^{-9}	1.63×10^{-14}	~43 min
2	340 K	10^{-3} mbar	N/A	3.20×10^{-8}	$(3.00\text{-}2.70)\times10^{-12}$	~29 min, dif. spot
3	335 K	0.01 mbar	N/A	$(2.90\text{-}3.20)\times10^{-7}$	5.00×10^{-11}	~29 mins, dif. spot
4	330 K	0.05 mbar	2.44×10^{-2}	$(4.58\text{-}4.68)\times10^{-7}$	6.70×10^{-11}	~29 mins, dif. spot
5	327 K	0.10 mbar	1.10×10^{-1}	$(1.06\text{-}1.00)\times10^{-6}$	$(1.49\text{-}1.48)\times10^{-10}$	~29 mins, dif. spot
6	323 K	0.15 mbar	$(1.60\text{-}1.55)\times10^{-1}$	1.49×10^{-6}	2.25×10^{-10}	~29 mins, dif. spot
7	321 K	0.20 mbar	$(2.03\text{-}2.08)\times10^{-1}$	1.92×10^{-6}	3.00×10^{-10}	~29 mins, dif. spot
8	319 K	0.4 mbar	$(4.07\text{-}3.87)\times10^{-1}$	$(3.73\text{-}3.59)\times10^{-6}$	6.00×10^{-10}	~42 mins, dif. Spot
9	317 K	1 mbar	1.03	1.06×10^{-5}	1.55×10^{-9}	~42 mins, dif. spot

Table 3.

No.	Sample temperature	Target pressure	NAP cell pressure (mbar)	NAP lens pressure (mbar)	QMS 18 AMU – H_2O (A)	X-ray exposure time
1	299 K	UHV (NAP cell)	N/A	5×10^{-9}	1×10^{-13}	~ 28 min
2	299 K	10^{-3} mbar	N/A	(2.19-1.68) $\times10^{-8}$	(3.1-2.27) $\times10^{-12}$	~25 min, dif. spot
3	299 K	0.01 mbar	N/A	(1.1-1.13) $\times10^{-7}$	(2.80-2.86) $\times10^{-11}$	~25 mins, dif. spot
4	299 K	0.10 mbar	1.02×10^{-1}	(6.24-5.5) $\times10^{-7}$	(1.86-1.76) $\times10^{-10}$	~25 mins, dif. spot
5	299 K	0.05 mbar	6.51×10^{-2}	2.28×10^{-7}	(5.9-5.72) $\times10^{-11}$	~27 mins, dif. spot
6	299 K	0.15 mbar	1.55×10^{-1}	1.13×10^{-6}	3.58×10^{-10}	~32 mins, dif. spot
7	299 K	0.20 mbar	2.28×10^{-1}	1.95×10^{-6}	6.48-6.41$\times10^{-10}$	~32 mins, dif. spot
8	299 K	0.4 mbar	4.03×10^{-1}	3.89×10^{-6}	1.28×10^{-9}	~32 mins, dif. spot
9	299 K	1 mbar	1.03-0.985	(1.43-1.36) $\times10^{-5}$	(3.19-3.01) $\times10^{-9}$	~32 mins, dif. spot

In Figure 4.28 the experiment results of the measurement are shown for the O 1*s* spectra (Measurement No. 1, 3, and No. 5-9 – some of the data are left out because of the insignificant changes in the spectrum). In a) subfigure the classical layer, in b) the gradual layer, and in c) the redox layer is visible.

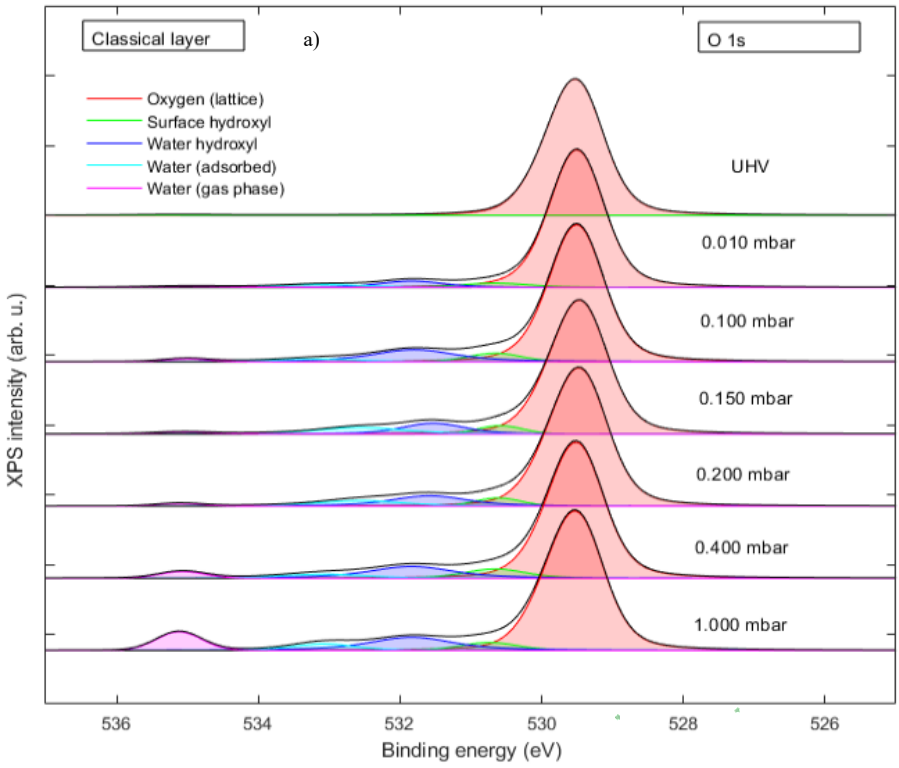
Classical layer
a)
O 1s
Oxygen (lattice)
Surface hydroxyl
Water hydroxyl
Water (adsorbed)
Water (gas phase)
UHV
0.010 mbar
0.100 mbar
0.150 mbar
0.200 mbar
0.400 mbar
1.000 mbar
XPS intensity (arb. u.)
536
534
532
530
528
526
Binding energy (eV)

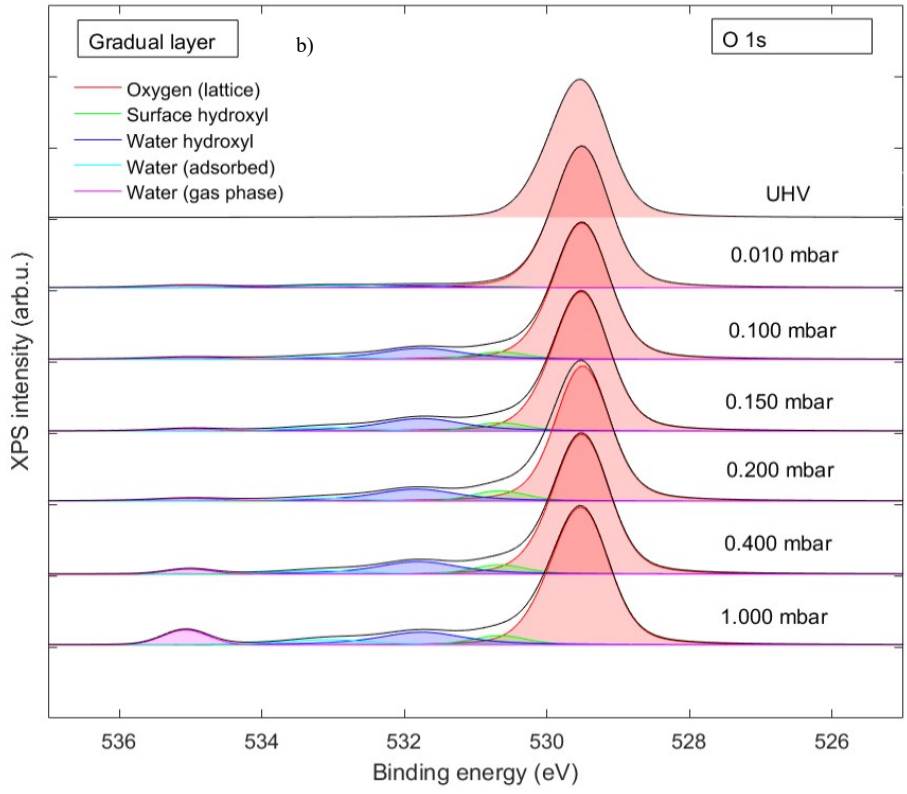
Gradual layer
b)
O 1s
Oxygen (lattice)
Surface hydroxyl
Water hydroxyl
Water (adsorbed)
Water (gas phase)
UHV
0.010 mbar
0.100 mbar
0.150 mbar
0.200 mbar
0.400 mbar
1.000 mbar
XPS intensity (arb.u.)
536
534
532
530
528
526
Binding energy (eV)

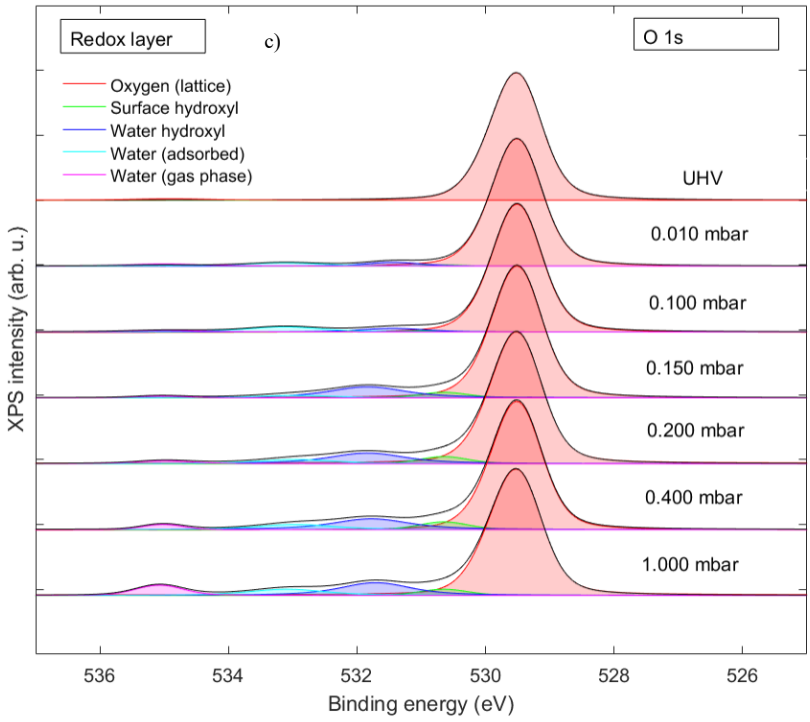

Figure 4.28: O 1*s* core level spectra of the water vapor interaction with three prepared CeO_2(111)/Pt(111) surface.

It is observable that by increasing the H_2O vapor pressure, the H_2O gas-phase peak is also increasing (marked with magenta color) at the binding energy ~535 eV. Considering the nature of water vapor interaction with CeO_2(111), three types of O 1*s* peaks are fitted: the molecularly adsorbed H_2O molecules (marked with cyan color) at binding energy 533 eV, surface hydroxyls O_sH (marked with green color) at binding energy around 531 eV, and water hydroxyl O_wH (from dissociated water molecules) at binding energy around 532 eV (marked with blue color). The oxygen lattice from CeO_2 is marked with red color at binding energy at ~ 529.5 eV, and serves as a reference peak, it shows that during the measurement its changes are negligible.

In Figure 4.29 the surface hydroxyl, the quantity of water hydroxyl, and the adsorbed molecular water are compared within the three layers in the format of adsorbed monolayers. In the graphs, the designated peak percentage of the whole measured O 1*s* spectra is illustrated in water vapor pressure dependence.

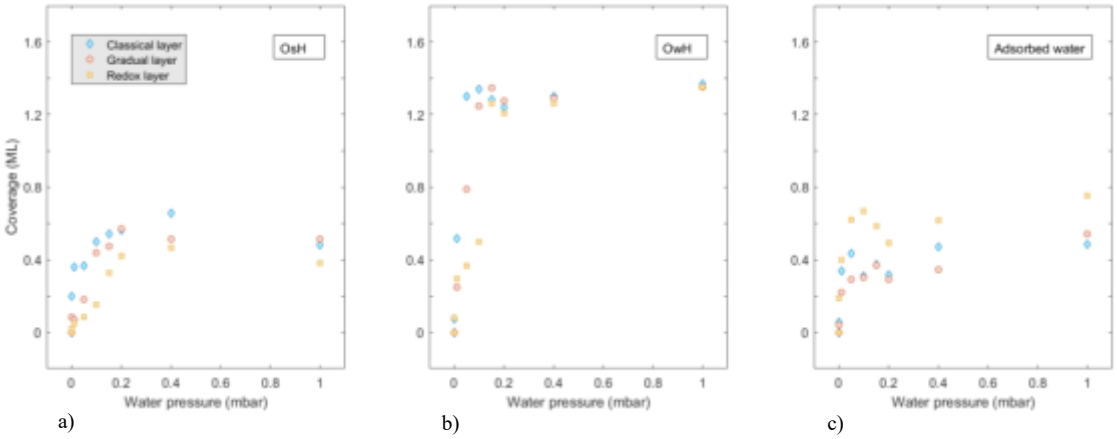

Figure 4.29: Monolayer (ML) coverage of surface hydroxyl (O_sH), water hydroxyl (O_wH), and adsorbed molecular water as the increase of water vapor pressure.

The density of step edges on the ceria surface was adjusted to establish a quantitative correlation between step density and water dissociation at the near ambient pressure. The first experiments for the three different models were conducted under UHV conditions, and no water adsorption was observed at room temperature due to the extensive cleaning procedures of the NAP cell systems. However, when the water pressure was increased above 0.01 mbar at RT, water adsorption was observed with the formation of surface hydroxyl groups.

At the lowest water vapor pressure, the amount of O_sH coverage varied significantly for the gradual, classical, and redox layers, with values of 0.20 ML, 0.08 ML, and 0.02 ML, respectively. The extent of water dissociation was 10 times more enhanced on the classical layer than on the redox layer. However, there was a saturation plateau between 0.2 to 1.0 mbar H_2O pressure where the coverage of dissociated O_sH on all three surfaces reached a similar amount of 0.5 ML regardless of their morphology. The O_wH coverage followed the trend of O_sH before the saturation pressure under 0.2 mbar, with the thickness of ML coverage declining in the order of classical > gradual > redox. Above 0.2 mbar, the O_wH reached the same plateau with a coverage of ~ 1.3 ML. The amount of molecular adsorbed water H_2O was consistently larger on redox layers than on the gradual and classical layers. At 1 mbar, the final H_2O adsorbed thickness on gradual and classical layers remained 0.5 ML, while it was 0.75 ML on the redox layer.

The total thickness of adsorbent species remained similar for all three layers, with a value of 2.40 ± 0.07 ML.

The reactivity of CeO_2(111) surfaces with different densities of step edges was found to be different. The density of step edges on the classical layer was observed to be twice as much (~10%) as on the redox layer (~5%), which leads to a lower dissociation threshold pressure for water than the redox layer. However, even though the step edges are more reactive, the coverage of dissociated OH groups on all three layers was the same at 1.82 ± 0.07 ML at 1 mbar of H_2O exposure. This suggests that the coverage of dissociated OH groups on CeO_2(111) surfaces is not step-edge dependent and only the vapor pressure related to the water dissociation threshold is dependent on the density of the step edges.

In brief, the experimental results suggest that CeO_2(111) surfaces with different densities of step edges display varied reactivities. Notably, water dissociation was observed to be more favorable on step edges compared to terraces.

In Figure 4.30 the changes in the Ce 3*d* peak are visible during the experiment. The experimental data (scattered grey plot), the fitted peaks and the sum fit (magenta, cyan, yellow, orange) of all the fitted peaks are visible (marked with the black curve). In subfigure a) the classical layer, b) the gradual layer, and in c) the redox layer is shown. As described before, the doublets at main peak energy 880.8 eV and 885.8 eV (very low peak intensity) represent the Ce^{3+} phase of the ceria layer, and the other three doublets (highlighted with magenta, cyan and yellow) represent the Ce^{4+} phase. The intensity of the Ce^{3+} phase doublets indicate how much is the CeO_2 layer reduced. It is visible that during the experiment all three layers reduced a bit. The amount of reduction is evaluated in Figure 4.31. where the taken percentage by the Ce^{3+} phase doublets of the whole measured Ce 3*d* spectra is illustrated in pressure dependence.

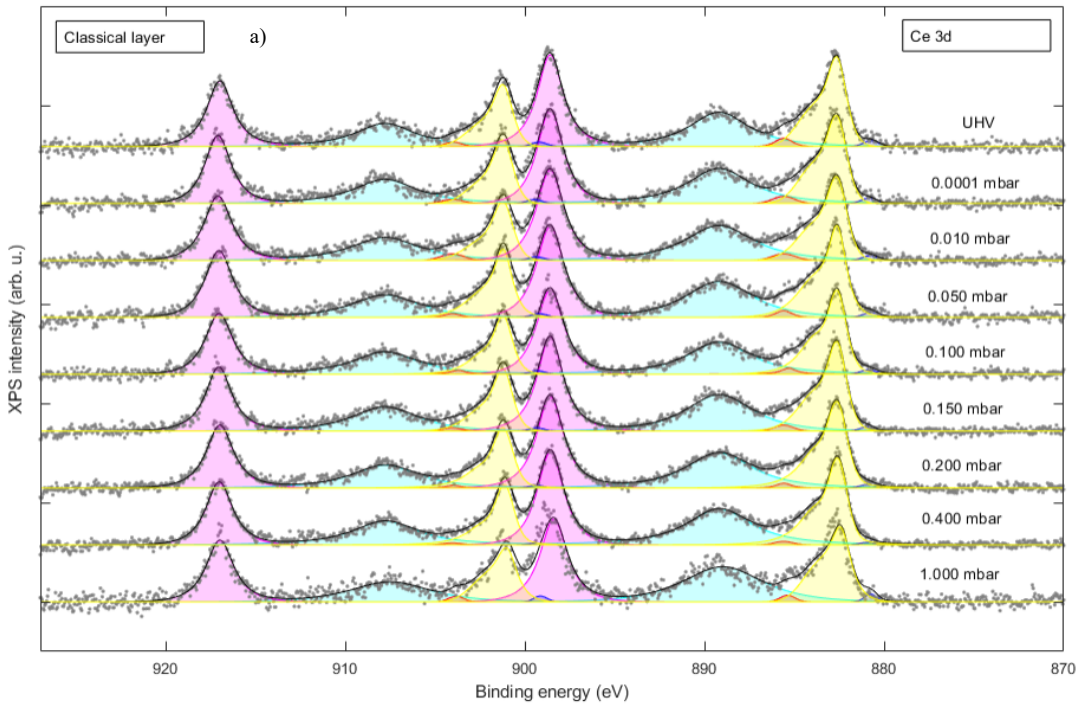
Classical layer
a)
Ce 3d
UHV
0.0001 mbar
0.010 mbar
0.050 mbar
0.100 mbar
0.150 mbar
0.200 mbar
0.400 mbar
1.000 mbar
XPS intensity (arb. u.)
920
910
900
890
880
870
Binding energy (eV)

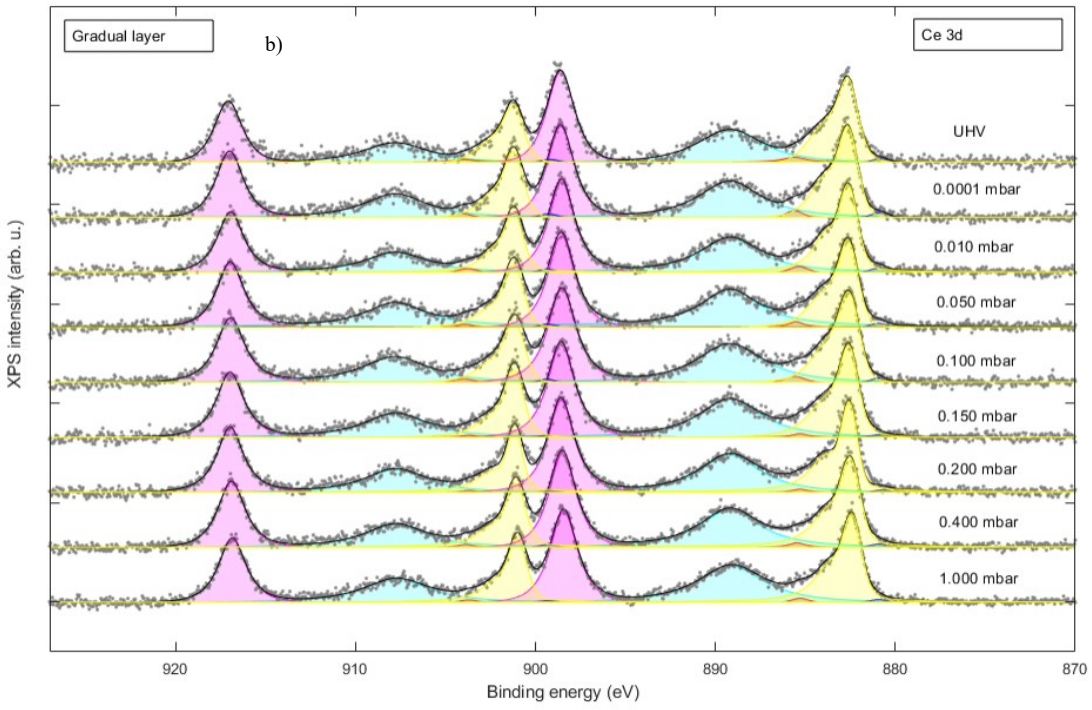
Gradual layer
b)
Ce 3d
UHV
0.0001 mbar
0.010 mbar
0.050 mbar
0.100 mbar
0.150 mbar
0.200 mbar
0.400 mbar
1.000 mbar
XPS intensity (arb. u.)
920
910
900
890
880
870
Binding energy (eV)

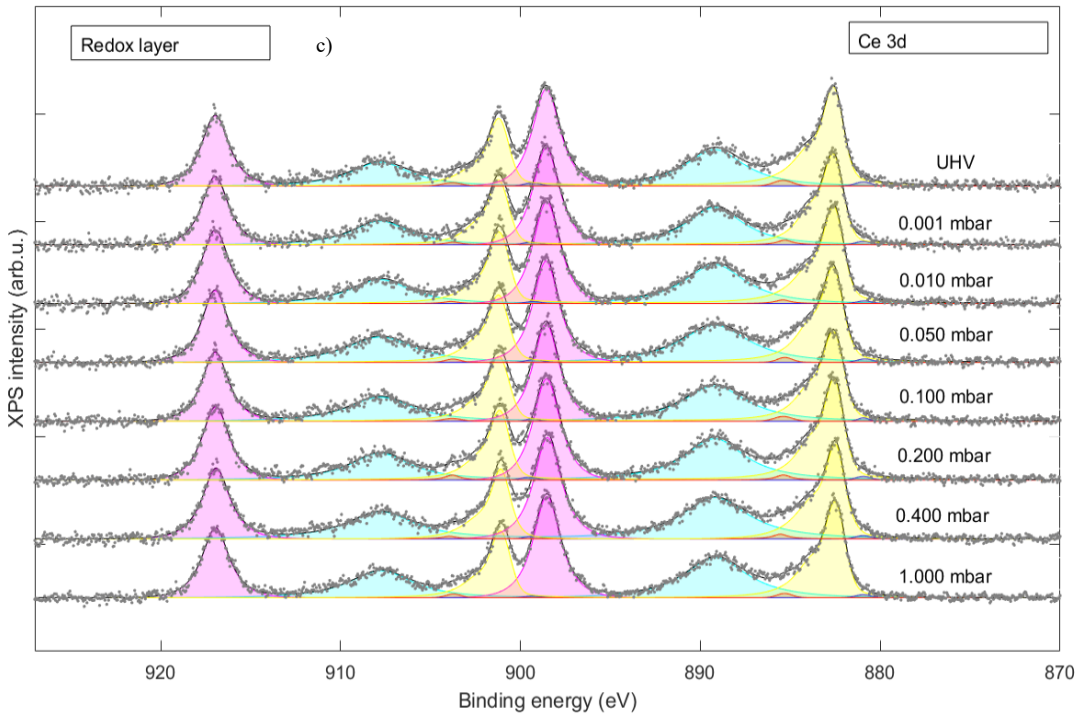

Figure 4.30: The Ce 3*d* spectra of the water vapor interaction with three prepared CeO_2(111) surfaces.

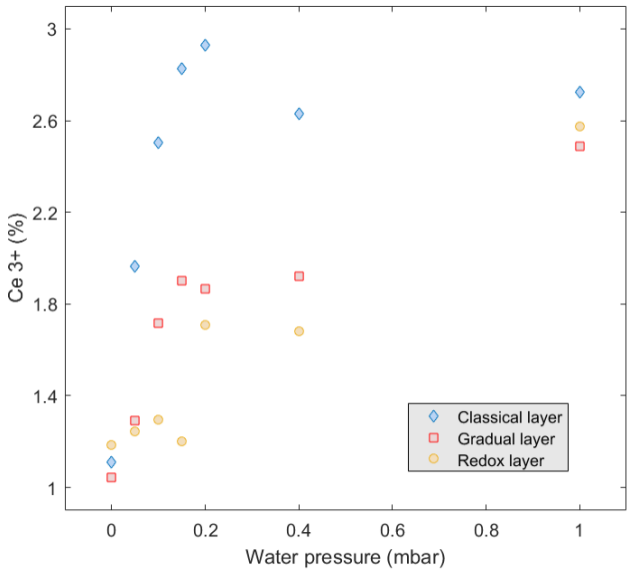

Figure 4.31: Ce^{3+} percentage in the presence of increased H_2O pressure.

From Figure 4.31 is obvious that all three layers initially had 1.1 (± 0.1) % of Ce^{3+} centers and 2.6 (± 0.1) % of Ce^{3+} at 1 mbar of H_2O pressure. However, the rate of reduction among the three layers is comparable to the rate of water dissociation. For reduced or partially reduced CeO_x surfaces, both experimental and theoretical studies showed that water tends to reduce ceria rather than re-oxidize it, at least under the conditions that have been examined. Matolín et al. reported a decrease in the ceria oxidation state induced by water for stoichiometric CeO_2(111). In our observations, we found a significant increase in Ce^{3+} centers when liquid water was deposited on the cerium oxide surface. The reduction effect caused by water on ceria under ambient conditions is likely due to the formation of hydroxide species from water dissociation, but further investigation is necessary.

In Figure 4.32 the C 1*s* peak for the classical layer is illustrated. There is no carbon observable on the scans within the equipment's error range. It is safe to claim that the layer used during the experiment was not contaminated. This also means that there was no contamination effect during the measurement that caused the reduction of cerium dioxide surface. For the other two layers, the scans were similar, the XPS showed negligible carbon contamination.

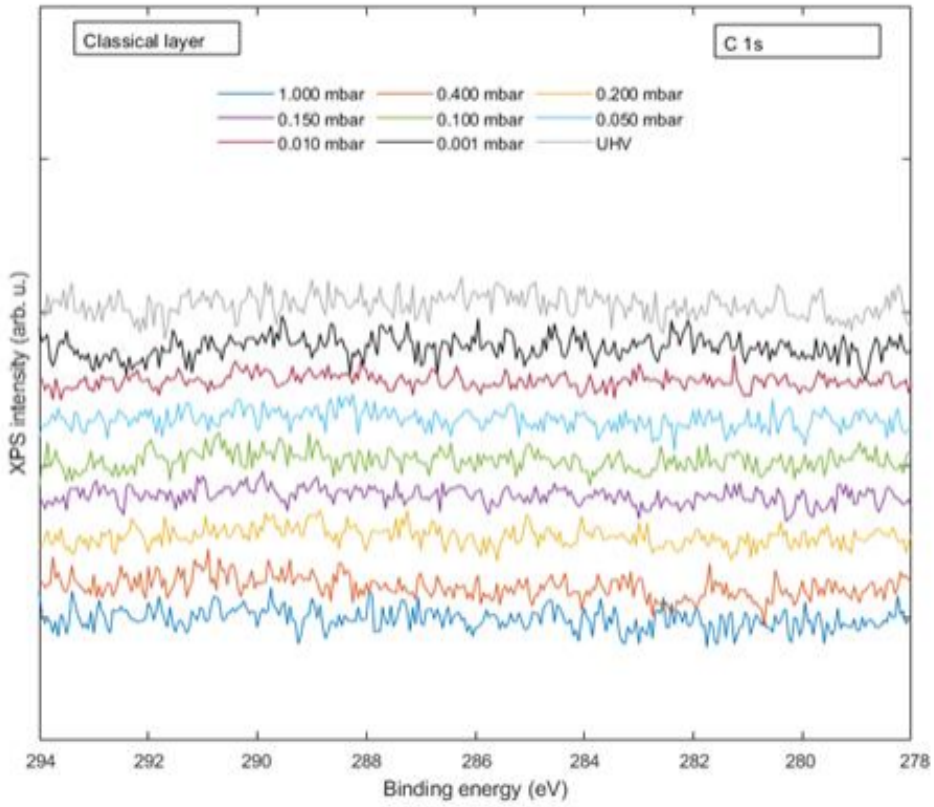

Figure 4.32: The C 1*s* core level spectra during the water adsorption experiment.

Conclusion

In this thesis, we have studied the role of step edges in water dissociation for three developed CeO_2(111)/Pt(111) model systems with controlled density of "defect sites" on the surface (step edges) by NAP-XPS technique under operando conditions. The phenomena seem to be an important step in most catalytic reactions. Three adsorption species on the cerium oxide surface were observed during the water experiment: surface hydroxyls water hydroxyls, and adsorbed water molecules.

One of the species, the surface hydroxyl (O_sH) saturated almost independently on the step edge density. The amount of coverage is slightly different (from the most coverage in order: classical, gradual, and redox), and the saturated value for all layers was around 0.5 ML. The saturation of the water hydroxyl (O_wH) happened a bit differently, for the classical layer was the fastest, followed by the gradual and the redox layer. The incorporation stopped at around 0.2 mbar when the coverage reached about 1.3 ML for every layer. The water adsorption was consistently larger for the redox layer (0.75 ML), while the adsorption in the case of classical and gradual layer stopped near 0.5 ML.

During the experiment, a small amount of reduction happened, which can be seen from the calculated percentage of Ce^{3+} doublets from the whole Ce 3*d* core level spectra. From the three models, the redox layer reduced the least, and the classical layer reduced the most and it happened until the water vapor pressure reached approximately 0.2 mbar, after which the reduction of the surface stopped.

The experiment proved that water molecules prefer to dissociate at step edges. The step edge density influences dissociation kinetics and determines the dissociation pressure threshold. However, the structures did not influence the maximum amount of water dissociation, the interaction stopped when the hydration coverage reached 1.82 ± 0.07 ML at 1 mbar of H_2O exposure above the dissociation pressure threshold.

According to the present study, the water-ceria interaction could be applied in catalytic reactions. Our investigation yielded valuable insights into the role of step edges in the

process of water dissociation and the effect of water hydroxylation/hydration on stoichiometric CeO_2 surfaces. These findings may provide the basis for reassessing the significance of step edges in this process.

Bibliography

[1] H. Seyama, M. Soma, B. K. G. Theng, Developments in Clay Science **2013**, 161–176.

[2] Matematicko-fyzikální fakulta Univerzity Karlovy, "Near-ambient-pressure X-ray and ultraviolet photoelectron spectroscopies", can be found under *https://nano.mff.cuni.cz/nanomaterials-group/instruments/near-ambient-pressure-x-ray-and-ultraviolet-photoelectron-spectroscopies*, **2021**.

[3] Jung, H.; Kittelson, D. B.; Zachariah, M. R. The influence of a cerium additive on ultrafine diesel particle emissions and kinetics of oxidation. Combustion and Flame **2005**, 142 (3), 276-288. DOI: 10.1016/j.combustflame.2004.11.015.

[4] Hajjiah, A.; Samir, E.; Shehata, N.; Salah, M. Lanthanide-Doped Ceria Nanoparticles as Backside Coaters to Improve Silicon Solar Cell Efficiency. Nanomaterials (Basel) **2018**, 8 (6). DOI: 10.3390/nano8060357.

[5] Korsvik, C.; Patil, S.; Seal, S.; Self, W. T. Superoxide dismutase mimetic properties exhibited by vacancy engineered ceria nanoparticles. Chemical Communications **2007**, (10), 1056-1058. DOI: 10.1039/B615134E.

[6] Rozhin, P.; Melchionna, M.; Fornasiero, P.; Marchesan, S. Nanostructured Ceria: Biomolecular Templates and (Bio)applications. Nanomaterials (Basel) 2021, 11 (9). DOI: 10.3390/nano11092259

[7] X. Ju, M. Hubalek Kalbacova, B. Šmíd, V. Johánek, M. Janata, T. N. Dinhová, T. Bělinová, M. Mazur, M. Vorokhta, L. Strnad, J. Mater. Chem. B **2021**, 9, 7386–7400.

[8] A. S. Karakoti, S. Singh, A. Kumar, M. Malinska, S. V. N. T. Kuchibhatla, K. Wozniak, W. T. Self, S. Seal, J. Am. Chem. Soc. **2009**, 131, 14144–14145.

[9] C. Korsvik, S. Patil, S. Seal, W. T. Self, Chem. Commun. **2007**, 1056.

[10] J. Carrasco, D. López-Durán, Z. Liu, T. Duchoň, J. Evans, S. D. Senanayake, E. J. Crumlin, V. Matolín, J. A. Rodríguez, M. V. Ganduglia-Pirovano, Angew. Chem. Int. Ed. **2015**, 54, 3917–3921.

[11] N. Nilius, S. M. Kozlov, J.-F. Jerratsch, M. Baron, X. Shao, F. Viñes, S. Shaikhutdinov, K. M. Neyman, H.-J. Freund, ACS Nano **2012**, 6, 1126–1133.

[12] Tsud, N.; Acres, R. G.; Iakhnenko, M.; Mazur, D.; Prince, K. C.; Matolin, V. Bonding of histidine to cerium oxide. Journal of Physical Chemistry B **2013**, 117 (31), 9182-9193. DOI: 10.1021/jp404385h

[13] Y. Lykhach, V. Johánek, H. A. Aleksandrov, S. M. Kozlov, M. Happel, T. Skála, P. St. Petkov, N. Tsud, G. N. Vayssilov, K. C. Prince, K. M. Neyman, V. Matolín, J. Libuda, J. Phys. Chem. C **2012**, 116, 12103–12113.

[14] V. Matolín, I. Matolínová, F. Dvořák, V. Johánek, J. Mysliveček, K. C. Prince, T. Skála, O. Stetsovych, N. Tsud, M. Václavů, B. Šmíd, Catalysis Today **2012**, 181, 124–132.

[15] S. Oregon, "The History of XPS", can be found under *https://xpslibrary.com/history-of-xps/*, **2019**.

[16] B. Šmíd, Příprava a studium katalytického systému Cu(O)-CeO_2 metodami povrchové analýzy, Doctoral thesis, Charles University, **2013**

[17] "X-ray photoelectron spectroscopy", can be found under https://en.wikipedia.org/wiki/X-ray_photoelectron_spectroscopy, **2023**.

[18] P. Dlabaja, Studium kovových povrchů za operando podmínek pomocí vysokotlaké skenovací tunelové mikroskopie, Bachelor thesis, Charles University, **2021**.

[19] A. Singh, T. Quach, "Wave-Particle Duality ", can be found under *https://chem.libretexts.org/Bookshelves/Physical_and_Theoretical_Chemistry_Textbook_Maps/Supplemental_Modules_(Physical_and_Theoretical_Chemistry)/Quantum_Mechanics/02._Fundamental_Concepts_of_Quantum_Mechanics/Wave-Particle_Duality*

[20] Y. Shi, Linköping Studies in Science and Technology. Dissertations **2019**, DOI 10.3384/diss.diva-159100.

[21] P. Wolfgang, S. Helmut. Apparatus for separating charged particles of different specific charges **1960**. US 2939952.

[22] T. Adamo, "Quadrupoles: How do they work?", can be found under *https://www.utsc.utoronto.ca/~traceslab/PDFs/MassSpec_QuadsInfo.pdf*, **2020**.

[23] PhysicsOpenLab, "Tunnel Effect", can be found under *https://physicsopenlab.org/2017/05/30/tunnel-effect/*, **2017**.

[24] "Scanning tunneling microscope", can be found under *https://en.wikipedia.org/wiki/Scanning_tunneling_microscope*, **2023**.

[25] Kolibrik.net, s.r.o., Czech Republic, "KolXPD", can be found under *https://www.kolibrik.net/en/kolxpd*

[26] S. Tougaard, Journal of Vacuum Science & Technology A **2021**, 39, 011201.

[27] "Voigt profile", can be found under *https://en.wikipedia.org/wiki/Voigt_profile*, **2023**

[28] F. Dvořák, O. Stetsovych, M. Steger, E. Cherradi, I. Matolínová, N. Tsud, M. Škoda, T. Skála, J. Mysliveček, V. Matolín, J. Phys. Chem. C **2011**, 115, 7496–7503.

[29] T. Duchoň, F. Dvořák, M. Aulická, V. Stetsovych, M. Vorokhta, D. Mazur, K. Veltruská, T. Skála, J. Mysliveček, I. Matolínová, V. Matolín, J. Phys. Chem. C **2013**, 118, 357–365.

[30] F. Dvořák, Interaction of simple molecules with reducible oxides: model studies of H2O/CeOx and CO/CuOx, Dissertation thesis, Charles University, **2014**

[31] D. R. Mullins, Surface Science Reports **2015**, 70, 42–85.

List of Tables

List of Abbreviations

STM – Scanning tunneling microscopy

LEED – Low energy electron diffraction

QMS – Quadrupole mass spectrometry

XPS – X-ray photoelectron spectroscopy

NAP – Near ambient pressure

NAP-XPS – Near ambient pressure X-ray photoelectron spectroscopy

UHV – Ultra - high vacuum

OSC – Oxygen storage capacity

ML – Monolayer

RT – Room temperature